ISSN 1364-5021 | Volume 472 | Issue 2186 | February 2016

PROCEEDINGS OF THE ROYAL SOCIETY A

MATHEMATICAL, PHYSICAL AND ENGINEERING SCIENCES

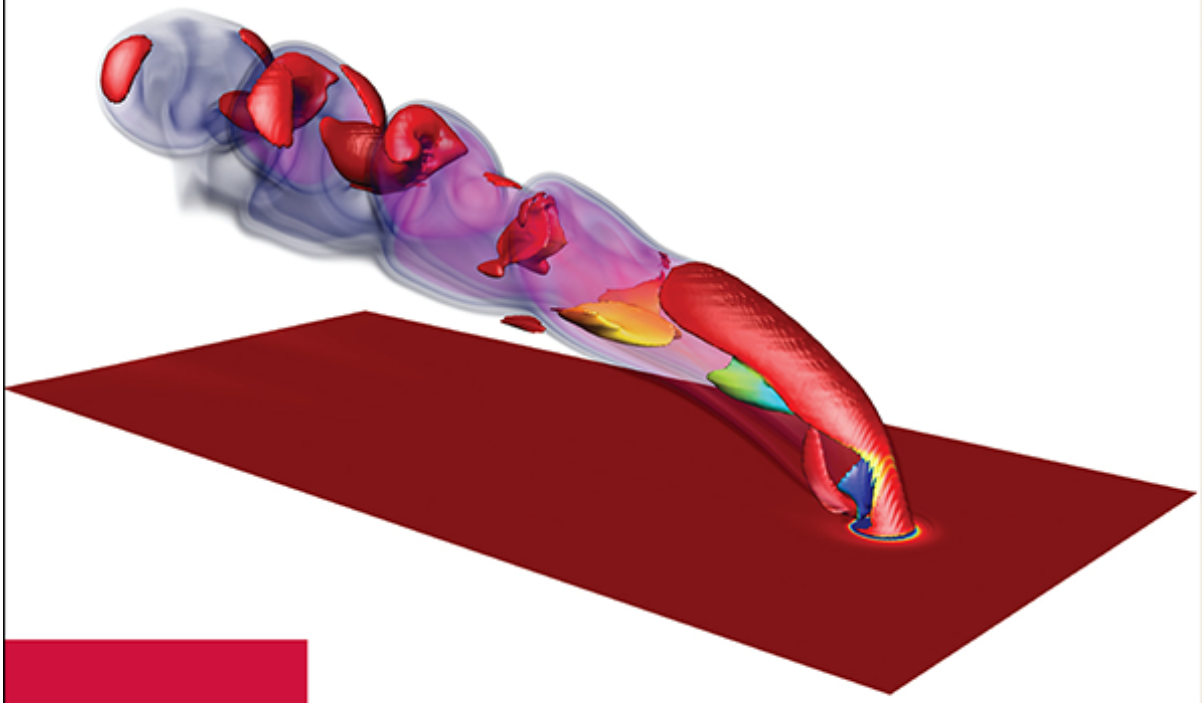

THE ROYAL SOCIETY PUBLISHING

PROCEEDINGS A

rspa.royalsocietypublishing.org

Research

Cite this article: Babaee H, Sapsis TP. 2016 A minimization principle for the description of modes associated with finite-time instabilities. *Proc. R. Soc. A* **472**: 20150779. http://dx.doi.org/10.1098/rspa.2015.0779

Received: 9 November 2015
Accepted: 11 January 2016

Subject Areas:
chaos theory, fluid mechanics

Keywords:
transient dynamics, finite-time instabilities, time-dependent modes, non-normal growth, dimension reduction

Author for correspondence:
T. P. Sapsis
e-mail: sapsis@mit.edu

A minimization principle for the description of modes associated with finite-time instabilities

H. Babaee[1,2] and T. P. Sapsis[1]

[1]Department of Mechanical Engineering, and [2]MIT Sea Grant College Program, Massachusetts Institute of Technology, Cambridge, MA 02139, USA

TPS, 0000-0003-0302-0691

We introduce a minimization formulation for the determination of a finite-dimensional, time-dependent, orthonormal basis that captures directions of the phase space associated with transient instabilities. While these instabilities have finite lifetime, they can play a crucial role either by altering the system dynamics through the activation of other instabilities or by creating sudden nonlinear energy transfers that lead to extreme responses. However, their essentially transient character makes their description a particularly challenging task. We develop a minimization framework that focuses on the optimal approximation of the system dynamics in the neighbourhood of the system state. This minimization formulation results in differential equations that evolve a time-dependent basis so that it optimally approximates the most unstable directions. We demonstrate the capability of the method for two families of problems: (i) linear systems, including the advection–diffusion operator in a strongly non-normal regime as well as the Orr–Sommerfeld/Squire operator, and (ii) nonlinear problems, including a low-dimensional system with transient instabilities and the vertical jet in cross-flow. We demonstrate that the time-dependent subspace captures the strongly transient non-normal energy growth (in the short-time regime), while for longer times the modes capture the expected asymptotic behaviour.

THE ROYAL SOCIETY PUBLISHING

1. Introduction

A broad range of complex systems in Nature and technology are characterized by the presence of strongly transient dynamical features associated with finite-time instabilities. Examples include turbulent flows in engineering systems (e.g. Kolmogorov [1] and unstable plane Couette flow [2], reactive flows in combustion [3,4]), turbulent flows in geophysical systems (e.g. climate dynamics [5,6], cloud processes in tropical atmospheric convection [7,8]), nonlinear waves (e.g. in optics [9,10] or water waves [11–14]) and mechanical systems [15–19].

These systems are characterized by very high-dimensional attractors, intense nonlinear energy transfers between modes and broad spectra. Despite their complexity, the transient features of these dynamical systems are often associated with low-dimensional structures, i.e. a small number of modes, whose strongly time-dependent character, however, makes it particularly challenging to describe with the classical notion of time-independent modes. This is because these modes, despite their connection with intense energy transfers and transient dynamics, often have low energy and hence they are 'buried' in the complex background of modes that are not associated with intense growth or decay but only with important energy. These transient modes often act as 'triggers' or 'precursors' of higher energy phenomena or instabilities and a thorough analysis of their properties can have important impact for (i) the understanding of the system dynamics and in particular the mechanisms associated with transient features (e.g. [20–22]), (ii) the prediction and quantification of upcoming instabilities that are triggered through these low-energy dynamical processes (e.g. [14,23,24]), and (iii) the control and suppression of these instabilities by suitably focusing the control efforts in the low-energy regime of these transient phenomena (e.g. [25–27]).

Transient dynamics is central in understanding a wide range of fluid mechanics problems. In the context of hydrodynamic stability, non-normality of the linearized Navier–Stokes operator can cause significant *transient energy growth* [28,29]. It is well established now that the eigenvalue analysis based on the largest real-part eigenvalue is unsuitable to predict the short-time evolution of perturbations for convective flows [30]. Instead, the transient energy growth can be better understood by analysing the pseudospectra of the linearized operator [31,32]. Transition from laminar flow to turbulence is another active area of research in fluid mechanics, for which understanding the transient dynamical features is crucial. For a finite-amplitude disturbance, *bypass transition* has been observed in wall-bounded shear flows [33,34], in which case the non-normal growth of localized disturbances leads to small turbulent spots, bypassing the secondary instability process [35]. Recent computational and experimental studies also demonstrate the *sudden transition* from laminar to turbulent motion in pipe flows, where turbulence forms from localized patches called *puffs* [36,37]. On the other hand, intermittent behaviour is the hallmark of turbulent fluid flows. Turbulent *chaotic bursts* appearing in spatially and temporally localized events can dramatically change the dynamics of the system [38]. Prototype systems that mimic these properties were introduced and analysed in [15,39–41]. Transient dynamics have a fundamental role in the intermittent behaviour of passive tracers as well, where even elementary models without positive Lyapunov exponents [42,43] have been able to reproduce intermittent behaviour observed in complex models. For such systems, the fundamental role of the random resonance between Fourier modes of the turbulent velocity field and the passive tracer has been recently illustrated [44].

In the context of uncertainty quantification and prediction a new family of stochastic methods relying on the so-called Dynamical Orthogonality condition was recently developed to deal with the strongly transient features of stochastic systems. Dynamically Orthogonal (DO) field equations [45,46] and dynamically bi-orthogonal (BO) equations [47] evolve a subspace according to the system stochastic PDE and the current statistical state of the system. Despite their success in resolving low-dimensional stochastic attractors for PDEs [48–50], these methodologies are often too expensive to implement for high-dimensional systems (e.g. DO or BO equations require the simultaneous solution of many PDEs) and have important limitations in systems characterized by intense energy transfers between modes [51–53]. In addition, in order to obtain

an accurate description of the time-dependent dynamics, many modes should be included in the analysis and the computational cost increases very rapidly (especially for systems with high complexity). These important limitations have been tackled using blended approaches that combine the time-dependent adaptive modes with appropriate nonlinear closures in a stochastic framework appropriate for uncertainty quantification [52,54,55] and filtering [53,56] of turbulent dynamical systems.

Our aim in this work is to develop a method that will generate adaptively a time-dependent basis that will capture strongly transient phenomena along a given (deterministic) trajectory of the system. This approach will rely on system observables obtained through either high-fidelity numerical solvers or measurements, as well as the linearized equations of the system. The core of our approach is a minimization principle that will seek to minimize the distance between the local vector field of the system, constrained over the direction of the time-dependent modes, and the rate of change of the time-dependent modes. A direct minimization of the defined functional will result in evolution equations for the optimally time-dependent (OTD) basis elements. For systems characterized by transient responses, these modes will adapt according to the (independently) computed or measured system history in a continuous way, capturing at each time the transiently most unstable directions of the system. For sufficiently long times where the system reaches an equilibrium, we prove that the developed equations provide the most unstable directions of the system in the asymptotic limit.

We demonstrate the developed approach over a series of applications, including linear and nonlinear systems. As a first example, we consider the advection–diffusion operator where we show how the OTD basis captures the directions associated with the non-normal behaviour. The second example involves the Orr–Sommerfeld/Squire operator that governs the evolution of infinitesimal disturbances in parallel viscous flows. Our goal here is also the computation of time-dependent modes that explain the transient growth of energy due to non-normal dynamics. The third problem involves a low-dimensional dynamical system as well as the nonlinear transient dynamics of a jet in cross-flow. Using the developed framework, we compute the modes associated with the transient but also asymptotically unstable directions of the phase space and we assess their time-dependent stability properties.

2. Optimally time-dependent basis for transient instabilities

Let the dynamical system

$$\dot{z} = F(z, t),$$

defined on a state space $A \subset \mathbb{R}^n$. We denote by $S_t(z_0)$ the position of the trajectory at time t that is initiated on z_0. Also, let

$$\dot{u} = L(S_t, t)u, \quad \text{with} \quad L(z, t) = \nabla_z F(z, t), \tag{2.1}$$

denote the linearized dynamical system around the trajectory S_t and let the inner product between two elements z_1 and z_2 be denoted as $z_1 \cdot z_2$. The linear time-dependent dynamical system represented by the above equation has the solution

$$u(t) = \Phi_{t_0}^t u(t_0), \tag{2.2}$$

where $\Phi_{t_0}^t$ is the propagator that maps the state of the system at time t_0 to t. The propagator can be represented as the ordered product of infinitesimal propagators

$$\Phi_{t_0}^t = \lim_{\delta t \to 0} \prod_{j=1}^{m} e^{L(S_{t_j}, t_j)\delta t}, \tag{2.3}$$

where t_j lies in $t_0 + (j-1)\delta t < t_j < t_0 + j\delta t$ and as $\delta t \to 0$, $m \to \infty$ such that $t = t_0 + m\delta t$. Our aim is to evolve a basis u_i, $i = 1, \ldots, r$, i.e. a set of time-dependent, orthonormal modes, so that $u_i(t)$ optimally follows $\Phi_{t_0}^t u_i(t_0)$ for all times. To achieve this goal, we formulate the following

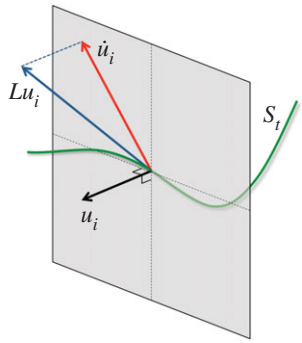

Figure 1. Illustration of the distance function $\mathcal{F}$ used to define the time-dependent modes. (Online version in colour.)

quantity, which measures the distance between the action of infinitesimal propagator $e^{L(S_{t_j},t_j)\delta t}$ on an orthonormal basis $u_i(t)$ and $u_i(t+\delta t)$. We have

$$\mathcal{F} = \lim_{\delta t \to 0} \frac{1}{(\delta t)^2} \sum_{i=1}^{r} \|u_i(t+\delta t) - \Phi_t^{t+\delta t} u_i(t)\|^2, \tag{2.4}$$

where $U(t) = [u_1(t), u_2(t), \ldots, u_r(t)]$ is an arbitrary and time-dependent orthonormal basis, i.e. for every time instant it satisfies the orthonormality condition

$$u_i(t) \cdot u_j(t) = \delta_{ij}, \quad i, j = 1, \ldots, r. \tag{2.5}$$

The above orthonormality condition given by equation (2.5) serves as a constraint on functional $\mathcal{F}$ expressed in equation (2.4). We observe that, in the functional given by equation (2.4),

$$u_i(t+\delta t) = u_i(t) + \delta t \dot{u}_i + \mathcal{O}(\delta t^2)$$

and

$$\Phi_t^{t+\delta t} = e^{L(S_t,t)\delta t} = I + \delta t L(S_t, t) + \mathcal{O}(\delta t^2),$$

where I is the identity matrix. Replacing the above equations into the functional given by equation (2.4) results in

$$\mathcal{F}(\dot{u}_1, \dot{u}_2, \ldots, \dot{u}_r) = \sum_{i=1}^{r} \left\| \frac{\partial u_i(t)}{\partial t} - L(S_t, t) u_i(t) \right\|^2. \tag{2.6}$$

In figure 1, we illustrate the distance function $\mathcal{F}$. For each direction u_i, we have, due to the normalization property $\|u_i\| = 1$, the rate of change $\dot{u}_i$ lying in the orthogonal complement of u_i. Under this constraint, we choose as $\dot{u}_i$ the vector that is closest to the image of u_i under the effect of the operator L.

We emphasize that the minimization of the function (2.6) is considered only with respect to the time derivative (rate of change) of the basis, $\dot{U}(t)$, instead of the basis $U(t)$ itself. This is because we do *not* want to optimize the subspace that the operator is acting on, but rather find an optimal set of vectors, $\dot{U}(t)$, that best approximates the linearized dynamics in the subspace U. We then solve the resultant equations and compute $U(t)$. We will refer to these modes as the OTD modes, and the space that these modes span as the OTD subspace.

Note that a direct minimization of the function (2.6), over finite-time intervals, with respect to the modes $U(t)$, would result in the well-known Euler–Lagrange equations. However, in this case, the emphasis is put on finding the optimal 'input' to the operator L in order for the function (2.6) to be minimized, while here our aim is different, i.e. we seek to find an optimal set of vectors that approximate L in the best possible way, when L is acting on U.

To summarize the above discussion, we are considering the following minimization problem:

For a trajectory S_t find $\dot{U}(t)$ such that $\mathcal{F}(\dot{U})$ is minimized.

In the reminder of this paper, we will demonstrate that this minimization principle allows us to capture any arbitrary and transient kind of growth caused by the linear operator, e.g. non-normal or exponential. In what follows, we obtain a differential formulation for the evolution equations that correspond to the proposed minimization problem.

(a) Evolution equations for the time-dependent modes

Before we proceed to the minimization of the function given by equation (2.6), we express the orthonormality constraints for the basic elements in terms of their time derivatives. By differentiating over time, we have

$$\frac{\partial u_i(t)}{\partial t} \cdot u_j(t) + \frac{\partial u_j(t)}{\partial t} \cdot u_i(t) = 0, \quad i,j = 1,\ldots,r. \tag{2.7}$$

The above condition is satisfied if the following condition is valid:

$$\frac{\partial u_i(t)}{\partial t} \cdot u_j(t) = \varphi_{ij}(t), \tag{2.8}$$

where $\varphi_{ij}(t)$ is any arbitrary function for which $\varphi_{ij} = -\varphi_{ji}$. Clearly, for any choice of $\varphi_{ij}(t)$, the above condition guarantees that if $\{u_i(t_0)\}_{i=1}^r$ is initially orthonormal, it will remain orthonormal for all times. As we will see the choice of φ_{ij} does not change the evolved subspace. However, it allows for different formulations of the evolution equations. Using the constraint (2.8), we have the following theorem.

Theorem 2.1. *The minimization principle* (2.6) *defined within the basis elements that satisfy the constraint* (2.8) *is equivalent to the set of evolution equations*

$$\frac{\partial u_k(t)}{\partial t} = L(S_t,t)u_k(t) - \sum_{j=1}^{r}(L(S_t,t)u_k(t)\cdot u_j(t) - \varphi_{kj}(t))u_j(t), \quad k = 1,\ldots,r, \tag{2.9}$$

where φ_{ij} is an arbitrary function for which $\varphi_{ij} = -\varphi_{ji}$.

Proof. We first formulate the minimization problem that also takes into account the appropriate number of Lagrange multipliers, $\lambda_{ij}(t)$,with $i,j = 1,\ldots,r$. In this way we obtain:

$$\mathcal{G}_\varphi(\dot{U}(t); L(S_t,t)) = \sum_{i=1}^{r}\left(\frac{\partial u_i(t)}{\partial t} - L(S_t,t)u_i(t)\right)^2 + \sum_{i,j=1}^{r}\lambda_{ij}(t)\left(\frac{\partial u_i(t)}{\partial t}\cdot u_j(t) - \varphi_{ij}(t)\right). \tag{2.10}$$

We consider the first derivative with respect to each $\dot{u}_i(t)$ to obtain the set of equations

$$\frac{\partial \mathcal{G}_\varphi}{\partial \dot{u}_k} = 2\left(\frac{\partial u_k(t)}{\partial t} - L(S_t,t)u_k(t)\right) + \sum_{j=1}^{r}\lambda_{kj}(t)u_j(t).$$

To obtain an extremum, we need the right-hand side of the last equation to vanish:

$$\frac{\partial u_k(t)}{\partial t} = L(S_t,t)u_k(t) - \frac{1}{2}\sum_{j=1}^{r}\lambda_{kj}(t)u_j(t), \tag{2.11}$$

which should be solved together with condition (2.8). We take the inner product of equation (2.11) with mode $u_l(t)$ and obtain

$$\frac{\partial u_k(t)}{\partial t}\cdot u_l(t) = L(S_t,t)u_k(t)\cdot u_l(t) - \frac{\lambda_{kl}(t)}{2} = \varphi_{kl}(t).$$

Using the last equation and substituting $\lambda_{kl}(t)$ in (2.11) will result in the evolution equations (2.9). This completes the proof. ■

In a more compact form, the evolution equation for a finite-dimensional operator $L \in \mathbb{R}^{n\times n}$ can be obtained, where we express the OTD subspace in a matrix $U \in \mathbb{R}^{n\times r}$ whose ith column is u_i. The function φ_{ij} is correspondingly expressed in the matrix notation as $\Phi \in \mathbb{R}^{r\times r}$ with $\Phi = \{\varphi_{ij}\}_{i,j=1}^{r}$. Thus, the evolution equation for the OTD modes can be expressed as:

$$\frac{\partial U}{\partial t} = LU - U(U^{\mathrm{T}}LU - \Phi), \tag{2.12}$$

where $(\,)^{\mathrm{T}}$ denotes the transpose of a matrix.

Now we define the *reduced operator* $L_{\mathrm{r}}(t) \in \mathbb{R}^{r\times r}$ that is obtained by projecting the original operator onto the subspace $U(t)$. Thus,

$$L_{\mathrm{r}} = U^{\mathrm{T}}LU. \tag{2.13}$$

Therefore, the OTD equation could be equivalently expressed as:

$$\frac{\partial U}{\partial t} = LU - U(L_{\mathrm{r}} - \Phi). \tag{2.14}$$

In what follows, we will need the definition of equivalence between two subspaces.

Definition 2.1. The two OTD subspaces $U \in \mathbb{R}^{n\times r}$ and $W \in \mathbb{R}^{n\times r}$ are equivalent at time t if there exists a transformation matrix $R \in \mathbb{R}^{r\times r}$ such that $U(t) = W(t)R$, where R is an orthogonal rotation matrix, i.e. $R^{\mathrm{T}}R = I$.

In the following we show that the evolution of two OTD subspaces $U(t) \in \mathbb{R}^{n\times r}$ and $W(t) \in \mathbb{R}^{n\times r}$ under different choice of $\Phi(t)$, which are initially equivalent (at $t = 0$), will remain equivalent for every time $t > 0$, i.e. $U(t) = W(t)R(t)$, where $R(t) \in \mathbb{R}^{r\times r}$ is an orthogonal rotation matrix governed by the matrix differential equation:

$$\left.\begin{aligned} \frac{\mathrm{d}R}{\mathrm{d}t} &= R\Phi_U - \Phi_W R \\ \text{and} \qquad R(0) &= R_0, \end{aligned}\right\} \tag{2.15}$$

with $\Phi_U \in \mathbb{R}^{r\times r}$ and $\Phi_W \in \mathbb{R}^{r\times r}$ being the two different choices of Φ for the evolution of U and W, respectively, while R_0 is the initial orthogonal rotation matrix, i.e. $U(0) = V(0)R_0$. We first prove the following lemma.

Lemma 2.1. *The solution $R(t)$ to the matrix differential equation given by equation (2.15) remains an orthogonal rotation matrix for every time $t > 0$ given that the initial condition $R(0)$ is an orthogonal rotation, i.e. $R(0)^{\mathrm{T}}R(0) = I$, and Φ_U and Φ_W are skew-symmetric matrices.*

Proof. We show that $d(R^{\mathrm{T}}R)/\mathrm{d}t = 0$ for every $t > 0$:

$$\begin{aligned} \frac{d(R^{\mathrm{T}}R)}{\mathrm{d}t} &= \dot{R}^{\mathrm{T}}R + R^{\mathrm{T}}\dot{R} \\ &= (R\Phi_U - \Phi_W R)^{\mathrm{T}}R + R^{\mathrm{T}}(R\Phi_U - \Phi_W R) \\ &= -\Phi_U R^{\mathrm{T}}R + R^{\mathrm{T}}\Phi_W R + R^{\mathrm{T}}R\Phi_U - R^{\mathrm{T}}\Phi_W R \\ &= R^{\mathrm{T}}R\Phi_U - \Phi_U R^{\mathrm{T}}R. \end{aligned}$$

Clearly $R^{\mathrm{T}}R = I$ is a fixed point for the above equation. ■

Next, we prove that, for a given dynamical system, the OTD subspaces that are initially equivalent remain equivalent for all times.

Theorem 2.2. *Suppose that $U(t) \in \mathbb{R}^{n\times r}$ and $W(t) \in \mathbb{R}^{n\times r}$ satisfy the evolution equation (2.12) with different choices of $\Phi(t)$ functions denoted by $\Phi_U(t) \in \mathbb{R}^{r\times r}$ and $\Phi_W(t) \in \mathbb{R}^{r\times r}$, respectively. We also assume that the two bases are initially equivalent, i.e. $U(0) = W(0)R_0$, where $R_0 \in \mathbb{R}^{r\times r}$ is an orthogonal rotation matrix. Then the subspaces $U(t)$ and $W(t)$ are equivalent for $t > 0$, with a rotation matrix $R(t) \in \mathbb{R}^{r\times r}$ governed by the matrix differential equation (2.15).*

Proof. We plug $U(t) = W(t)R(t)$ into the OTD equation for $U(t)$:

$$\dot{W}R + W\dot{R} = LWR - WR(R^{\mathrm{T}}W^{\mathrm{T}}LWR - \Phi_U).$$

Multiplying both sides from the right with R^{T}, and using the identity $RR^{\mathrm{T}} = I$, results in:

$$\dot{W} = LW - W(W^{\mathrm{T}}LW - R\Phi_U R^T + \dot{R}R^{\mathrm{T}}).$$

Now we substitute $\dot{R}$ from equation (2.15) into the above equation to obtain:

$$\dot{W} = LW - W(W^{\mathrm{T}}LW - \Phi_W),$$

which is the evolution equation for the OTD basis $W(t)$. This completes the proof. ■

Theorem 2.2 implies that the difference between the two bases will evolve along directions already contained in the initially common subspace. To this end, both bases will continue to span the same subspace and the variation between the two is only an internal rotation. Therefore, the two families of equations will result in the same time-dependent subspace. There are multiple choices for the function φ_{ij} and we now examine a special one.

(i) The dynamically orthogonal formulation

The simplest choice for the function φ in (2.8) is $\varphi_{ij} = 0$ for all i, j. The resultant evolution equations in this case will have the form

$$\frac{\partial U}{\partial t} = QLU, \tag{2.16}$$

where $Q := I - UU^{\mathrm{T}}$ is the orthogonal projection operator onto the subspace U. Note that $\varphi_{ij} = 0$ corresponds to the DO condition [45,48] that has been employed to derive closed equations for the solution of stochastic PDEs. In this case, uncertainty is resolved only along specific modes that evolve with time by projecting the original equation of the system over these directions. The evolution of these modes (stochastic subspace) is done according to equations derived using the DO condition and they have the general form of system (2.16). The equivalence of system (2.16) with the minimization problem (2.6) provides a clear interpretation for the evolution of the DO modes.

(b) Steady linearized dynamics

Here, we consider the special case where L is a time-independent operator. We prove that the basis defined through the introduced minimization principle will asymptotically span the eigenvectors of L *associated with the most intense instabilities* (i.e. eigenvalues with largest real part). In particular, we have the following theorem.

Theorem 2.3. *Let $L \in \mathbb{R}^{n\times n}$ be a steady and diagonalizable operator that represents the linearization of an autonomous dynamical system. Then*

(*i*) *Equation* (2.16) *has $\binom{n}{r} = n!/(n-r)!r!$ equilibrium states that consist of all the r-dimensional subspaces in the span of r distinct eigenvectors of L.*

(*ii*) *From all the equilibrium states, there is only one that is a stable solution for equation* (2.16). *This is given by the subspace spanned by the eigenvectors of L associated with the r eigenvalues having the largest real part.*

Proof. Let $L\Phi = \Phi\Lambda$, where Φ is the matrix of eigenvectors of the operator L with the column of $\Phi \in \mathbb{R}^{n\times n}$ being the eigenvectors: $\Phi = \{\phi_1|\phi_2|\cdots|\phi_n\}$, and $\Lambda \in \mathbb{R}^{n\times n}$ is the diagonal eigenvalue matrix whose entries are: $\Lambda = \mathrm{diag}(\lambda_1, \lambda_2, \ldots, \lambda_n)$.

(i) First, we show that a subspace U_0 that is in the span of precisely r eigenvectors of the operator L is an equilibrium state for equation (2.16). Without loss of generality, we consider the first r eigenvectors to span such a space, i.e. $U_0 \in \Phi_r = \mathrm{span}\{\phi_1|\phi_2|\cdots|\phi_r\}$ associated

with $\Lambda_r = \mathrm{diag}(\lambda_1, \lambda_2, \ldots, \lambda_r)$, and therefore U_0 can be expressed in eigenvector coordinates as: $U_0 = \Phi_r \kappa_0$ where $\kappa_0 \in \mathbb{R}^{r\times r}$ is the projection coefficient. Therefore, $LU_0 = L\Phi_r\kappa_0 = \Phi_r\Lambda_r\kappa_0 \in \mathrm{span}\{\phi_1|\phi_2|\cdots|\phi_r\}$. As a result, LU_0 is in the null space of the orthogonal projector Q, and thus $QLU_0 = 0$. This result is independent of the choice of eigenvectors. To this end, we note that, for an operator L with distinct eigenvalues, there exists a number of $\binom{n}{r} = n!/(n-r)!r!$ of such equilibrium states.

(ii) Next, we show that, from all the equilibrium states U_0, the subspace that is spanned by the eigenvectors associated with the largest eigenvalues is the only stable equilibrium. First, we investigate the stability of $U_0 \in \Phi_r$. We denote the complement of the space Φ_r with $\Phi_{r^c} = \mathrm{span}\{\phi_{r+1}|\phi_{r+2}|\cdots|\phi_n\}$ associated with the corresponding eigenvalues of $\Lambda_{r^c} = \mathrm{diag}(\lambda_{r+1}, \lambda_{r+2}, \ldots, \lambda_n)$. We consider a perturbation $U' \in \mathbb{R}^{n\times r}$ that belongs to the orthogonal complement of U_0, i.e. $U' \in U_0^C$,

$$U(t) = U_0 + \epsilon U'(t), \quad U'(t) \perp U_0.$$

We note that the orthonormality condition for $U(t)$, i.e. $U(t)^{\mathrm{T}}U(t) = I$, is satisfied for $\epsilon \ll 1$,

$$\begin{aligned} U(t)^{\mathrm{T}}U(t) &= (U_0 + \epsilon U'(t))^{\mathrm{T}}(U_0 + \epsilon U'(t)) \\ &= U_0^{\mathrm{T}}U_0 + \epsilon(U_0^{\mathrm{T}}U'(t) + U'(t)^{\mathrm{T}}U_0) + \epsilon^2 U'(t)^{\mathrm{T}}U'(t) \\ &= I + \epsilon^2 U'(t)^{\mathrm{T}}U'(t) \\ &\simeq I, \quad \text{for } \epsilon \ll 1. \end{aligned}$$

In the above equation, we use the orthonormality condition of $U' \perp U_0$ that implies: $U_0^{\mathrm{T}}U'(t) = U'(t)^{\mathrm{T}}U_0 = 0$. Moreover, since $U_0^{\mathrm{T}}U'(t) = 0$, we immediately obtain:

$$U_0^{\mathrm{T}}\frac{\partial U'(t)}{\partial t} = 0 \quad t \geq 0, \tag{2.17}$$

which requires the evolution of the perturbation, i.e. $\partial U'(t)/\partial t$, to remain orthogonal to U_0 for all times. Now, linearizing the evolution equation stated in equation (2.16) around the equilibrium state U_0 yields

$$\frac{\partial U'}{\partial t} = QLU' - U_0U'^{\mathrm{T}}LU_0 - U'U_0^{\mathrm{T}}LU_0.$$

In the above equation, the term $U'^{\mathrm{T}}LU_0 = 0$, since $LU_0 \in \mathrm{span}\{\phi_1|\phi_2|\cdots|\phi_r\}$ and $U' \perp U_0$. Therefore, the evolution equation for the perturbation equation becomes

$$\frac{\partial U'}{\partial t} = QLU' - U'U_0^{\mathrm{T}}LU_0. \tag{2.18}$$

Next, we transform the evolution equation (2.18) into the eigenvector coordinates. The perturbation U' can be expressed in eigenvector coordinates as: $U' = \Phi\kappa'$, where $\kappa' \in \mathbb{R}^{n\times r}$. Replacing $U_0 = \Phi_r\kappa_0$ and $U' = \Phi\kappa'$ into equation (2.18) results in

$$\Phi\frac{\mathrm{d}\kappa'}{\mathrm{d}t} = Q\Phi\Lambda\kappa' - \Phi\kappa'\kappa_0^{\mathrm{T}}\Phi_r^{\mathrm{T}}\Phi_r\Lambda_r\kappa_0. \tag{2.19}$$

Having assumed that L is non-deficient, we multiply both sides of equation (2.19) by Φ^{-1},

$$\begin{aligned} \frac{\mathrm{d}\kappa'}{\mathrm{d}t} &= \Pi\Lambda\kappa' - \kappa'\kappa_0^{\mathrm{T}}\Phi_r^{\mathrm{T}}\Phi_r\Lambda_r\kappa_0 \\ &= \Pi\Lambda\kappa' - \kappa'\kappa_0^{-1}\Lambda_r\kappa_0, \end{aligned} \tag{2.20}$$

where we introduced $\Pi = \Phi^{-1}Q\Phi$ and used the orthonormality condition of $U_0^{\mathrm{T}}U_0 = \kappa_0^{\mathrm{T}}\Phi_r^{\mathrm{T}}\Phi_r\kappa_0 = I$. We then multiply both sides by κ_0^{-1} to obtain

$$\frac{\mathrm{d}\rho'}{\mathrm{d}t} = \Pi\Lambda\rho' - \rho'\Lambda_r, \tag{2.21}$$

where $\rho' = \kappa' \kappa_0^{-1}$. The perturbation ρ' can be decomposed as

$$\rho' = \begin{pmatrix} \rho'_r \\ \rho'_{r_c} \end{pmatrix}, \tag{2.22}$$

where $\rho'_r \in \mathbb{R}^{r\times r}$ and $\rho'_{r^c} \in \mathbb{R}^{r^c\times r}$, with $r + r^c = n$. The matrix Π can be written as

$$\begin{aligned} \Pi &= I_{n\times n} - \Phi^{-1}\Phi_r \kappa_0 \kappa_0^{\mathrm{T}} \Phi_r^{\mathrm{T}} \Phi \\ &= I_{n\times n} - \Phi^{-1}\Phi_r \kappa_0 \kappa_0^{\mathrm{T}} \Phi_r^{\mathrm{T}} (\Phi_r \ \Phi_{r^c}). \end{aligned} \tag{2.23}$$

In the above equation, we note that

$$\Phi^{-1}\Phi_r = \begin{pmatrix} I_{r\times r} \\ 0_{r_c\times r} \end{pmatrix} \tag{2.24}$$

$$\begin{aligned} \kappa_0 \kappa_0^{\mathrm{T}} \Phi_r^{\mathrm{T}} (\Phi_r \ \Phi_{r^c}) &= (\kappa_0 \kappa_0^{\mathrm{T}} \Phi_r^{\mathrm{T}} \Phi_r \kappa_0 \kappa_0^{-1} \ \kappa_0 \kappa_0^{\mathrm{T}} \Phi_r^{\mathrm{T}} \Phi_{r^c}) \\ &= (I_{r\times r} \ \Theta_{r\times r_c}). \end{aligned} \tag{2.25}$$

In the last equation, we used the orthonormality condition of $U_0^{\mathrm{T}} U_0 = \kappa_0^{\mathrm{T}} \Phi_r^{\mathrm{T}} \Phi_r \kappa_0 = I$ and introduced $\Theta = \kappa_0 \ \kappa_0^{\mathrm{T}} \Phi_r^{\mathrm{T}} \Phi_{r^c}$. Replacing equations (2.24) and (2.25) into equation (2.23) results in

$$\Pi = \begin{pmatrix} 0_{r\times r} & \Theta_{r\times r_c} \\ 0_{r_c\times r} & I_{r_c\times r_c} \end{pmatrix}. \tag{2.26}$$

By replacing equation (2.26) into equation (2.21), the evolution equation becomes

$$\frac{\mathrm{d}}{\mathrm{d}t} \begin{pmatrix} \rho'_r \\ \rho'_{r_c} \end{pmatrix} = \begin{pmatrix} 0 & \Theta \Lambda_{r^c} \\ 0 & \Lambda_{r^c} \end{pmatrix} \begin{pmatrix} \rho'_r \\ \rho'_{r_c} \end{pmatrix} - \begin{pmatrix} \rho'_r \Lambda_r \\ \rho'_{r_c} \Lambda_r \end{pmatrix}. \tag{2.27}$$

The evolution equation for the perturbation must satisfy the orthogonality constraint $\partial U'(t)/\partial t \perp U_0$ expressed by equation (2.17). The orthogonality constraint requires that

$$U_0^{\mathrm{T}} \frac{\partial U'}{\partial t} = U_0^{\mathrm{T}} (QLU' - U' U_0^{\mathrm{T}} L U_0) = 0.$$

Since $U_0 \in \mathbb{R}^{n\times r}$, the above orthogonality condition, in fact, imposes r constraints on the evolution of perturbation $\rho'(t)$. In the following, we simplify these constraints. In the above equation

$$\begin{aligned} U_0^{\mathrm{T}} (QLU' - U' U_0^{\mathrm{T}} L U_0) &= \kappa_0^{\mathrm{T}} \Phi_r^{\mathrm{T}} (\Phi \Pi \Phi^{-1} \Phi \Lambda \kappa' - \Phi \kappa' \kappa_0^{\mathrm{T}} \Phi_r^{\mathrm{T}} \Phi_r \Lambda_r \kappa_0) \\ &= \kappa_0^{\mathrm{T}} \Phi_r^{\mathrm{T}} \Phi (\Pi \Lambda \kappa' - \kappa' \kappa_0^{-1} \Lambda_r \kappa_0) \kappa_0^{-1} \kappa_0 \\ &= \kappa_0^{\mathrm{T}} \Phi_r^{\mathrm{T}} \Phi (\Pi \Lambda \rho' - \rho' \Lambda_r) \kappa_0 \\ &= \kappa_0^{\mathrm{T}} \Phi_r^{\mathrm{T}} \begin{pmatrix} \Phi_r & \Phi_{r^c} \end{pmatrix} (\Pi \Lambda \rho' - \rho' \Lambda_r) \kappa_0 \\ &= \kappa_0^{-1} \begin{pmatrix} I_{r\times r} & \Theta_{r\times r_c} \end{pmatrix} (\Pi \Lambda \rho' - \rho' \Lambda_r) \kappa_0. \end{aligned}$$

Therefore, the orthogonality constraint $\partial U'(t)/\partial t \perp U_0$ is equivalent to

$$(I_{r\times r} \ \Theta_{r\times r_c})(\Pi \Lambda \rho' - \rho' \Lambda_r) = 0. \tag{2.28}$$

It follows that

$$\begin{pmatrix} I_{r\times r} & \Theta_{r\times r_c} \end{pmatrix} \begin{pmatrix} 0 & \Theta \Lambda_{r^c} \\ 0 & \Lambda_{r^c} \end{pmatrix} \begin{pmatrix} \rho'_r \\ \rho'_{r_c} \end{pmatrix} - \begin{pmatrix} I_{r\times r} & \Theta_{r\times r_c} \end{pmatrix} \begin{pmatrix} \rho'_r \Lambda_r \\ \rho'_{r_c} \Lambda_r \end{pmatrix} = 0, \tag{2.29}$$

or, equivalently,

$$\Theta \Lambda_{r_c} \rho'_{r_c} - \rho'_r \Lambda_r = \Theta (\rho'_{r_c} \Lambda_r - \Lambda_{r_c} \rho'_{r_c}). \tag{2.30}$$

Using the orthogonality constraint given by equation (2.30) and using equation (2.27), the evolution equation for $\rho'_r(t)$ becomes

$$\frac{\mathrm{d}\rho'_r}{\mathrm{d}t} = \Theta(\rho'_{r_c}\Lambda_r - \Lambda_{r_c}\rho'_{r_c}). \tag{2.31}$$

The above equation shows that the evolution of $\rho'_r(t)$ can be expressed solely based on the evolution of $\rho'_{r_c}(t)$. Thus, the stability of the solution only depends on the stability of ρ'_{r_c}. The evolution of ρ'_{r_c} in the index notation is given by

$$\frac{\mathrm{d}\rho'_{ij}}{\mathrm{d}t} = (\lambda_i - \lambda_j)\rho'_{ij}, \quad i = r+1, r+2, \ldots, n, \quad \text{and } j = 1, 2, \ldots, r. \tag{2.32}$$

Therefore, the asymptotic stability of ρ' requires that

$$\mathrm{real}(\lambda_i) \le \mathrm{real}(\lambda_j), \quad \text{for } i = r+1, r+2, \ldots, n, \quad \text{and} \quad j = 1, 2, \ldots, r. \tag{2.33}$$

The inequality (2.33) shows that the subspace Φ_r with eigenvalues having the largest real part is the only stable solution to equation (2.16). This completes the proof. ■

(c) Time-dependent linearized dynamics

Consider the evolution of an arbitrary (not orthonormal) subspace $V(t) \in \mathbb{R}^{n\times r}$ under the time-dependent linearized dynamics which is governed by

$$\left.\begin{aligned} \frac{\partial V}{\partial t} &= L(t)V \\ \text{and} \qquad V(0) &= V_0, \end{aligned}\right\} \tag{2.34}$$

and consider the corresponding OTD evolution

$$\left.\begin{aligned} \frac{\partial U}{\partial t} &= L(t)U - UL_r(t) \\ \text{and} \qquad U(0) &= U_0. \end{aligned}\right\} \tag{2.35}$$

We choose the initial state of the OTD basis such that U_0 and V_0 span the same subspace. In the following theorem, we show that the OTD modes exactly span the subspace $V(t)$. More specifically, we show that the two subspaces $U(t)$ and $V(t)$ are related via a time-dependent transformation matrix.

Theorem 2.4. *Let $V(t) \in \mathbb{R}^{n\times r}$ be the subspace evolved under the time-dependent linearized dynamics, equation (2.34), and $U(t) \in \mathbb{R}^{n\times r}$ be the OTD basis evolved with equation (2.35). Then, assuming that initially the two subspaces are equivalent, i.e. there is a matrix T_0 such that $V_0 = U_0T_0$, there exists a linear transformation $T(t)$ such that $V(t) = U(t)T(t)$, where $T(t)$ is the solution of the matrix differential equation*

$$\left.\begin{aligned} \frac{\mathrm{d}T(t)}{\mathrm{d}t} &= L_r(t)T(t) \\ \text{and} \qquad T(0) &= T_0. \end{aligned}\right\} \tag{2.36}$$

Proof. We substitute the transformation $V(t) = U(t)T(t)$ into the evolution equation for $V(t)$,

$$\dot{U}T + U\dot{T} = LUT.$$

Substituting $\dot{T}$ from equation (2.36) after rearrangement results in

$$\dot{U}T = LUT - UL_rT.$$

Multiplying both sides of the above equation by T^{-1} from the right results in

$$\dot{U} = LU - UL_r,$$

which is the OTD equation for $U(t)$. The initial condition is also $U(0) = U_0$. This completes the proof. ■

For dynamical systems with persistent instabilities, the evolution under the time-dependent linearized equation (2.34) is unstable, and $V(t)$ grows rapidly. Even for stable dynamical systems, as we move away from $t = 0$, almost any vector approaches the least stable direction. However, the evolution of the OTD modes, due to their built-in orthonormality, is always stable, and, as we will demonstrate in our results, the OTD evolution leads to a well-conditioned numerical algorithm that peels off the most unstable directions of the dynamics.

(d) Mode ranking within the subspace

Having derived the subspace that corresponds to the most unstable directions, the next step is to rank these directions internally, i.e. within the subspace. As we describe below, there are two ways to rank the OTD basis based on the growth rate. Both of these approaches amount to an internal rotation within the OTD subspace.

(1) The *instantaneous growth rate* $\sigma_i(t)$ [19,57] is obtained by computing the eigenvalues of the symmetric part of L_r, *i.e* $L_r^\sigma = (L_r + L_r^{\mathrm{T}})/2$,

$$L_r^\sigma R^\sigma = R^\sigma \Sigma, \tag{2.37}$$

where $\Sigma = \mathrm{diag}(\sigma_1(t), \sigma_2(t), \ldots, \sigma_r(t))$, and $R^\sigma(t) \in \mathbb{R}^{r\times r}$ is the matrix of eigenvectors. We rank these values from the least stable to the most stable directions, i.e.

$$\sigma_1(t) \geq \sigma_2(t) \cdots \geq \sigma_r(t).$$

We note that $\sigma_{\max}(t) = \sigma_1(t)$ is the *numerical abscissa* of the operator L_r. Therefore, $\sigma_{\max}(t)$ represents the maximum instantaneous growth rate within the OTD subspace.

(2) The *instantaneous eigenvectors* of the reduced operator can also be obtained through the equation

$$L_r R^\lambda = R^\lambda \Lambda_r, \tag{2.38}$$

where the eigendirections are represented by $R^\lambda(t) \in \mathbb{C}^{r\times r}$. The instantaneous eigenvalues are denoted by $\Lambda_r(t) = \mathrm{diag}(\lambda_1(t), \lambda_2(t), \ldots, \lambda_r(t))$, where λ_i are ranked from the eigenvalue with the largest real part $\lambda_1(t)$ to the eigenvalue with the smallest real part $\lambda_r(t)$.

Based on the above two rankings, we define the rotated OTD basis as

$$U^{\lambda,\sigma}(t) = U(t) R^{\lambda,\sigma}(t), \tag{2.39}$$

where $U^{\lambda,\sigma}(t) \in \mathbb{C}^{n\times r}$ is the ranked representation of the OTD modes defining the space U, and $R^{\lambda,\sigma}$ is the rotation matrix obtained from either of the two described strategies for mode ranking (equation (2.37) or equation (2.38)). For a non-Hermitian operator L, the ranking based on the instantaneous eigenvectors $R^\lambda(t)$ results in modes $U^{\lambda,\sigma}$, which may not be mutually orthogonal. For this case, the orthogonal representation of the least stable directions can be obtained by performing a Gram–Schmidt orthonormalization.

3. Linear dynamics

Linear dynamics, and in particular non-normal behaviour, has a critical role in determining the short-time fate of a disturbance in both linear and nonlinear dynamical systems. To study the evolution of an initial condition under the effect of linear or linearized dynamics, a reduction in eigenfunction coordinates is often used. However for highly non-normal operators, a large number of eigenfunctions are required to correctly capture the non-normal behaviour, since the eigenfunctions are far from orthogonal and, in fact, they constitute a highly ill-conditioned basis. In what follows we demonstrate the computational efficiency of the OTD modes in capturing non-normal behaviour and contrast the OTD basis with the eigenfunction basis for linear systems.

(a) Advection–diffusion operator

As the first case, we consider the advection–diffusion operator which has a wide range of applications in fluid mechanics, financial mathematics and many other fields. Particularly, we are interested to study the effect of non-normality on the reduced operator, in both the short-time and the long-term asymptotic behaviour. The operator with zero boundary condition is given by

$$\left.\begin{aligned} L(u) &= \nu \frac{\partial^2 u}{\partial x^2} + c\frac{\partial u}{\partial x}, \quad x \in [0,1] \\ \text{and} \qquad u(0,t) &= 0, \quad u(1,t) = 0, \end{aligned}\right\} \tag{3.1}$$

where ν is the diffusion coefficient and c is the advection speed. The evolution equation for the OTD basis is expressed by

$$\left.\begin{aligned} \frac{\partial u_i}{\partial t} &= L(u_i) - \langle L(u_i), u_j\rangle u_j, \quad i,j, = 1,\ldots,r \\ \text{and} \qquad u_i(0,t) &= 0, \quad u_i(1,t) = 0, \end{aligned}\right\} \tag{3.2}$$

where the inner product and the induced norm are

$$\langle u, v\rangle := \int_0^1 u(x)v(x)\,\mathrm{d}x, \quad \|u\| := \langle u, u\rangle^{1/2}.$$

To solve the evolution equation, we use Chebyshev collocation discretization implemented in Chebfun [58]. The OTD basis is initialized with orthonormalized modes

$$u_n(x,0) = \frac{\sin(n\pi x)}{\|\sin(n\pi x)\|}, \quad n = 1,2,\ldots,r,$$

for all the cases considered in this section.

In the case of a nearly normal operator, i.e. large ν, an optimal basis must be close to the dominant eigenfunctions for all times. On the other hand, for a set of parameters that corresponds to a non-normal operator, an optimal basis should differ from the eigenfunctions for short-time dynamics, and only for $t \gg 1$ should it converge to the operator eigenfunctions. In the remainder of this section, we demonstrate that the OTD subspace captures short- and long-time dynamics for both normal and non-normal operators.

To analyse the behaviour of the OTD basis, we choose $r = 4$. The instantaneous eigenvalues of the reduced operator, real($\lambda_i(t)$), for $\nu = 0.2$ are shown with coloured solid lines in figure 2*a*. The real part of the least stable eigenvalues of the operator L are shown with the dashed lines. It is clear that the instantaneous eigenvalues quickly approach the least stable eigenvalues of L. In figure 3*a*, the first two elements of the OTD basis, internally rotated in the eigendirection, ϕ_1 and ϕ_2, are shown at $t = 0.2$ and $t = 4.0$. These are superimposed with the two most unstable eigenfunctions of the operator. At $t = 0.2$ the modes are very close to the eigenfunctions of L, and at $t = 4.0$ the modes have essentially converged to the eigenfunctions. This demonstrates that, due to the strongly normal behaviour of the operator at $\nu = 0.2$, the eigenfunctions explain the dynamics accurately for both short time and long time, and the OTD basis quickly converges to the space spanned by the eigenfunctions.

At $\nu = 0.02$, however, the instantaneous eigenvalues converge with a much slower rate and much later, i.e. $t > 3$, to the operator eigenvalues, as shown in figure 2*b*. Accordingly, as can be seen in figure 3*b*, the OTD basis elements are different from the eigenfunctions of L at $t = 0.2$, and it is only later that the basis approaches the eigenfunctions. Another important observation is related to the advection direction of the OTD basis, which is left-ward. For instance at $t = 0.2$, the basis has advected an approximate distance of $\Delta x = c\Delta t = 0.2$ to the left. As a result, the OTD basis has a strong presence in the region $0 < x < 0.8$. This is not the case for the eigenfunctions of L, which are primarily concentrated near $x = 0$.

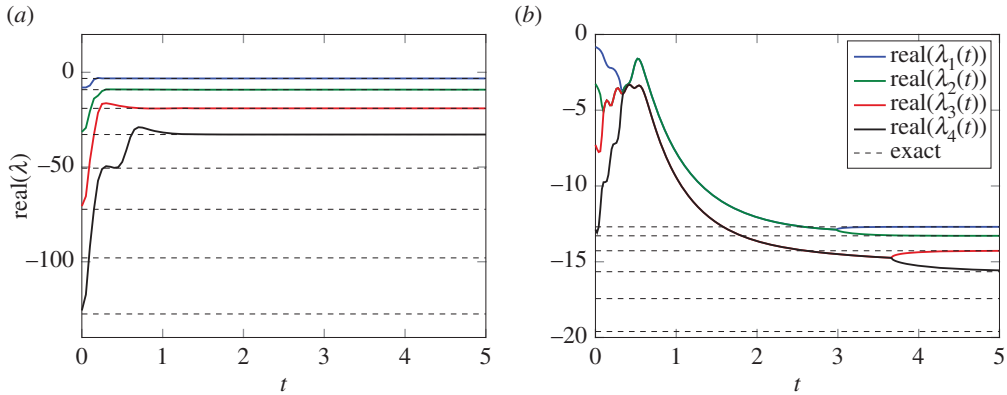

Figure 2. Instantaneous eigenvalues of the reduced operator with $r = 4$ for $c = 1$. The dashed lines show the eigenvalues of $\mathcal{L}$ with the largest real part. (*a*) $\nu = 0.2$; (*b*) $\nu = 0.02$. (Online version in colour.)

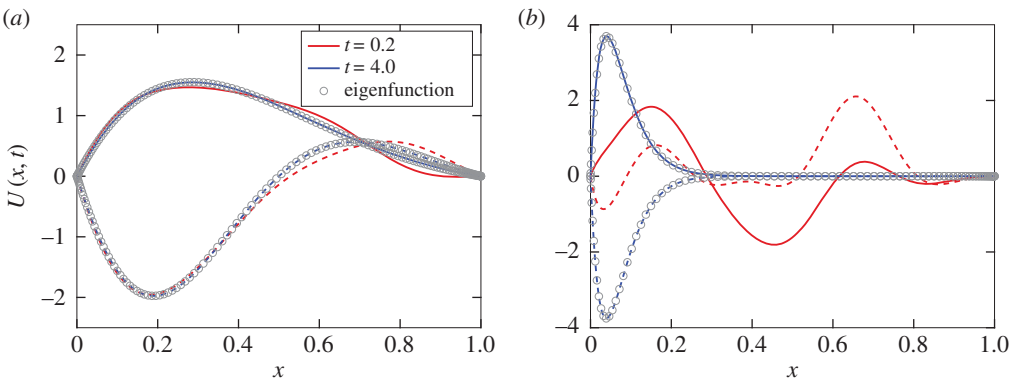

Figure 3. OTD basis for $r = 4$ and $c = 1$. The circles show the first two dominant eigenfunctions of L. The solid and dashed lines show the first and second OTD modes, i.e. $u_1^{\lambda}(x, t)$ and $u_2^{\lambda}(x, t)$: (*a*) $\nu = 0.2$; (*b*) $\nu = 0.02$. (Online version in colour.)

(b) Orr–Sommerfeld/Squire operator

As the second case, we consider the Orr–Sommerfeld/Squire (OS/SQ) equation that governs the evolution of infinitesimal disturbances in parallel viscous flows. The eigenvalues of the OS/SQ operator are highly sensitive to perturbations, and its eigenfunctions are linearly dependent, resulting in a highly ill-conditioned linear dynamical system. To this end, the OS/SQ equation is considered only for demonstration purposes, i.e. to illustrate that the OTD modes capture correctly the short-time evolution of the infinitesimal disturbances, as well as their asymptotic (long-term) behaviour.

We consider the plane Poiseuille flow in which the base-flow velocity is unidirectional and is given by $\mathbf{u}(x, y, z) = U(y)\mathbf{e}_x$, with $U(y) = 1 - y^2$. The disturbance is taken to be

$$\mathbf{v}'(x, y, z, t) = \mathbf{v}(y, t)\exp(\mathrm{i}\alpha x + \mathrm{i}\beta z),$$

with

$$\mathbf{v}' = \begin{pmatrix} v' \\ \eta' \end{pmatrix} \quad \text{and} \quad \mathbf{v} = \begin{pmatrix} v \\ \eta \end{pmatrix},$$

where v' and η' are the wall-normal velocity and the vorticity, respectively, and α and β denote the streamwise and spanwise wavenumbers, respectively.

The Orr–Sommerfeld equation in velocity–vorticity formulation is given by

$$\frac{\partial \mathbf{v}}{\partial t} = L\mathbf{v}, \tag{3.3}$$

with boundary conditions

$$v = \mathcal{D}v = \eta = 0 \quad \text{at} \quad y = \pm 1, \tag{3.4}$$

where L is a linear operator

$$L = \begin{pmatrix} L_{\mathrm{OS}} & 0 \\ L_{\mathrm{C}} & L_{\mathrm{SQ}} \end{pmatrix}, \tag{3.5}$$

with

$$L_{\mathrm{OS}} = (\mathcal{D}^2 - k^2)^{-1}\left[\frac{1}{Re}(\mathcal{D}^2 - k^2)^2 + \mathrm{i}\alpha\mathcal{D}^2 U - \mathrm{i}\alpha U(\mathcal{D}^2 - k^2)\right],$$

$$L_{\mathrm{C}} = -\mathrm{i}\beta\mathcal{D}U,$$

$$L_{\mathrm{SQ}} = \frac{1}{Re}(\mathcal{D}^2 - k^2) - \mathrm{i}\alpha\mathcal{D}U,$$

and $k = \sqrt{\alpha^2 + \beta^2}$ is the modulus of the wavevector and $\mathcal{D} = \partial/\partial y$. For the complete derivation of the OS/SQ equations, we refer to [59].

For the choice of the inner product, we use the energy measure, which provides a physically motivated norm that arises naturally from the OS/SQ equation [20]. The inner product is given by

$$\langle \mathbf{v}_1, \mathbf{v}_2 \rangle_E := \frac{1}{k^2}\int_{-1}^{1} \mathbf{v}_1^H M \mathbf{v}_2 \, \mathrm{d}y, \tag{3.6}$$

where

$$M = \begin{pmatrix} k^2 - \mathcal{D}^2 & 0 \\ 0 & 1 \end{pmatrix}, \tag{3.7}$$

and $(\,)^H$ denotes the complex conjugate. In the following, we consider a discrete representation of the operator $L \in \mathbb{C}^{n\times n}$. Assuming a solution of the form

$$\mathbf{v} = \boldsymbol{\phi} \exp \lambda t,$$

the initial value problem (3.3) transforms to an eigenvalue problem of the form

$$L\Phi = \Phi\Lambda,$$

where $\Lambda = \mathrm{diag}(\lambda_1, \lambda_2, \ldots, \lambda_n)$ and $\Phi = \{\phi_1 | \phi_2 | \cdots | \phi_n\}$ are, respectively, the matrices of the eigenvalues and the eigenvectors of L.

Orszag [60] showed that, for $Re \le Re_c \simeq 5772.22$, all eigenvalues of the operator L have negative real parts and therefore any perturbation is asymptotically stable. However, even for $Re < Re_c$, the energy of a perturbation may experience significant transient growth. This is a direct consequence of the non-normality of L. In this section, we look at the evolution of the OTD modes for the OS/SQ operator. In particular, we consider a three-dimensional perturbation with $\alpha = 1$ and $\beta = 1$ at $Re = 5000$, which corresponds to an asymptotically stable operator.

Since the dynamical system is linear, the linear tangent operator and L are identical. Thus, the evolution equation for the OTD modes $\mathbf{U} = \{\mathbf{u}_1, \mathbf{u}_2, \ldots, \mathbf{u}_r\}$ becomes

$$\frac{\partial \mathbf{u}_i}{\partial t} = L\mathbf{u}_i - \langle L\mathbf{u}_i, \mathbf{u}_j \rangle_E \mathbf{u}_j, \quad \mathbf{u}_i = \begin{pmatrix} v_i \\ \eta_i \end{pmatrix}, \quad i, j = 1, 2, \ldots, r, \tag{3.8}$$

with the boundary conditions

$$v_i = \mathcal{D}v_i = \eta_i = 0 \quad \text{at} \quad y = \pm 1, \; i = 1, 2, \ldots, r. \tag{3.9}$$

For space we use Chebyshev collocation discretization with 256 points, while for time advancement we use the first-order implicit Euler method.

(i) Initial condition

We initialize the OTD subspace such that its span encompasses the *optimal initial condition*: an initial condition $\mathbf{v}^0$ that reaches the maximum possible amplification at a given time $t = t_{\max}$. The optimal initial condition can be formulated as [20]

$$G(t_{\max}) = \max_{\mathbf{v}_0 \neq 0} \frac{\|\mathbf{v}(t_{\max})\|_E^2}{\|\mathbf{v}_0\|_E^2} = \|\exp(\Lambda t_{\max})\|_E^2. \tag{3.10}$$

The value of $\|\exp(\Lambda t_{\max})\|_E^2$ is equal to the principal singular value s_1 of the propagator $\boldsymbol{\Phi}_{t_0}^{t_{\max}} = \exp(L t_{\max})$. It follows that

$$\boldsymbol{\Phi}_{t_0}^{t_{\max}} \mathbf{V}_0 = \mathbf{V}\mathbf{S}, \tag{3.11}$$

where $\mathbf{V}(t_{\max}) = \{\mathbf{v}_1(t_{\max}), \ldots, \mathbf{v}_n(t_{\max})\}$ are the right singular eigenvectors and $\mathbf{V}_0 = \{\mathbf{v}_{1_0}, \mathbf{v}_{2_0}, \ldots, \mathbf{v}_{n_0}\}$ are the left singular eigenvectors, and $\mathbf{S} = \mathrm{diag}\{s_1, s_2, \ldots, s_n\}$ consists of singular values of the operator $\boldsymbol{\Phi}_{t_0}^{t_{\max}}$. In the above expression, $\mathbf{v}_i(t_{\max})$ corresponds to the state of the solution at $t = t_{\max}$ with the corresponding initial condition of $\mathbf{v}_{i_0}$. The initial state of the subspace of size r is chosen to be

$$\mathbf{u}_{i_0} = \mathbf{v}_{i_0}, \quad i = 1, \ldots, r.$$

The admissible initial conditions for the OTD modes must satisfy (i) the orthonormality constraint and (ii) the boundary conditions at the walls given by equation (3.9). It is straightforward to show that the above choice is compatible with these criteria. We also note that, short of these criteria, the choice of initial conditions for the OTD subspace is arbitrary. Certainly, the choice of optimal initial condition is of high practical importance, to which significant attention is paid in the literature. We refer readers to [20] and references therein. Moreover, due to the non-normality of the operator, the optimal initial condition requires a large number of eigenmodes for accurate representation, resulting in a relatively high-dimensional system in eigenmode coordinates compared with the OTD modes.

(ii) Transformation matrix

We obtain a time-dependent reduction of the OS/SQ operator by projecting L onto the OTD subspace using the energy inner product

$$L_{r_{ij}}(t) = \langle \mathbf{u}_i, L(\mathbf{u}_j) \rangle_E, \quad i, j = 1, \ldots, r, \tag{3.12}$$

where $L_r(t) \in \mathbb{C}^{r \times r}$ is the reduced OS/SQ operator. The reduced operator is then used to evolve the transformation matrix $T(t) \in \mathbb{C}^{r \times r}$ according to equation (2.36). Using the same initial condition $\mathbf{V}_0$ for both OTD modes and OS/SQ results in T_0 being the identity matrix, i.e. $T_0 = I$. In the following section, we compare the evolution of $\mathbf{V}_0$ under the full OS/SQ operator with the evolution of $\mathbf{V}_0$ using the transformation relation $\mathbf{V}(t) = \mathbf{U}(t)T(t)$.

(iii) Asymptotically stable subspace

We consider the evolution of the OTD subspace with $r = 2$ and $r = 3$ for three-dimensional perturbations at $Re = 5000$ and streamwise and spanwise wavenumbers of $\alpha = 1$ and $\beta = 1$. At this Reynolds number, all perturbations are asymptotically stable, while some perturbations experience significant non-normal growth in the short-time regime. In figure 4, the norm of the solution operator, $\|e^{Lt}\|_E^2$, is shown. As can be seen, the energy of some initial conditions is amplified by a factor of over 100. The maximum energy growth can be achieved at $t_{\max} = 25.06$ for the optimal initial condition. The optimal initial condition is obtained from equation (3.11). We initialize the two OTD modes with the first two elements of the right singular eigenvectors $\mathbf{V}_0$.

Now, we first compare the evolution of the initial subspace with $r = 2$ using the reduced operator with that of the full OS/SQ operator for the choice of initial condition explained in §3b(i). In figure 4, we compare the energy of $\mathbf{v}_1(t)$ and $\mathbf{v}_2(t)$ obtained from (i) evolution of the OTD and

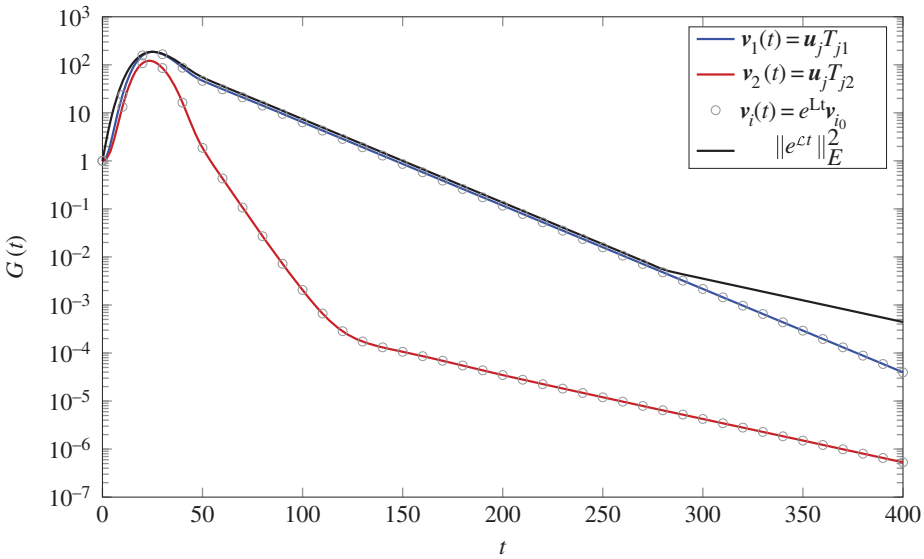

Figure 4. Transient energy growth, $G(t) = \|\mathbf{v}\|_E^2$, for plane Poiseuille flow at $Re = 5000$ with $\alpha = 1$ and $\beta = 1$. The solid lines (blue and red) show the energy growth of two different initial perturbations computed with the reduced operator with $r = 2$. The circles show the exact energy growth computed with the OS/SQ operator. (Online version in colour.)

using the transformation matrix $T(t)$ to obtain $\mathbf{v}_i(t) = \mathbf{u}_j(t)T_{ji}(t)$, $i, j = 1, \ldots, r$, and (ii) by solving the full OS/SQ operator, i.e. $\mathbf{v}_i(t) = \boldsymbol{\Phi}_0^t \mathbf{v}_{i_0} = e^{Lt}\mathbf{v}_{i_0}$. In both cases, excellent agreement in both short-time and long-time evolution is observed. This demonstrates that the OTD modes correctly follow the evolution of a class of initial conditions according to theorem 2.4. Given that, at $Re = 5000$, the OS/SQ operator is highly non-normal, a large number of eigenmodes are required to correctly follow the evolution of an initial condition. However, the OTD modes do not require additional modes beyond the dimension of the initial subspace.

In figure 5, the instantaneous eigenvalues for $r = 2$ along with numerical abscissa for $r = 2$ and $r = 3$ are shown. The black dashed lines show the real parts of the eigenvalues of the OS/SQ operator. The eigenvalues shown are the four most unstable ones of the OS/SQ operator. The significant non-normal energy growth manifests itself with positive real eigenvalues and instantaneous growth rates in finite time, despite all eigenvalues of OS/SQ having negative real parts. The instantaneous eigenvalues for the case with $r = 2$ converge to the first two least stable eigenvalues of the OS/SQ operator in accordance with theorem 2.3. For $r = 2$, the largest real instantaneous eigenvalue and the numerical abscissa $\sigma_{\max}$ are nearly identical. This shows that $\mathbf{u}_1(t)$ is nearly aligned with the direction of maximum growth for all times.

Now we explore some aspects of increasing the dimension of OTD from $r = 2$ to $r = 3$. For the sake of brevity, let us denote the quantities for the case $r = 3$ with the superscript $(\,)'$. The initial condition of the cases with $r = 2$ and $r = 3$ are $\mathbf{V}_0 = \{\mathbf{v}_{1_0}, \mathbf{v}_{2_0}\}$ and $\mathbf{V}_0' = \{\mathbf{v}_{1_0}, \mathbf{v}_{2_0}, \mathbf{v}_{3_0}\}$, respectively. Clearly, $\mathbf{V}_0 \subset \mathbf{V}_0'$ and consequently $\mathbf{V}(t) \subset \mathbf{V}'(t)$ for all times. From the transformation between $\mathbf{U}(t)$ and $\mathbf{V}(t)$, we can deduce that the embedding of the initial condition is preserved for the OTD subspaces as well, i.e. $\mathbf{U}(t) \subset \mathbf{U}'(t)$ for all times. Therefore, it is to be expected that the maximum growth rate in the case of $r = 3$ must always be larger than (or equal to) the corresponding value in the case of $r = 2$. In other words, $\sigma_{\max}(t) \leq \sigma'_{\max}(t)$ for all times. This observation is confirmed by comparing the numerical abscissa for $r = 2$ and $r = 3$ as shown in figure 5. The abrupt changes in the values of numerical abscissa are the result of eigenvalue crossing in the symmetric part of the reduced operator L_r, where the direction of maximum growth switches from one eigendirection to the other.

Figure 6 shows the OTD modes for the case of $r = 2$ at three time instants of their evolution at the streamwise plane $x = \pi$: (i) the initial state $t = 0$, (ii) maximum energy $t = t_{\max}$, and (iii) at

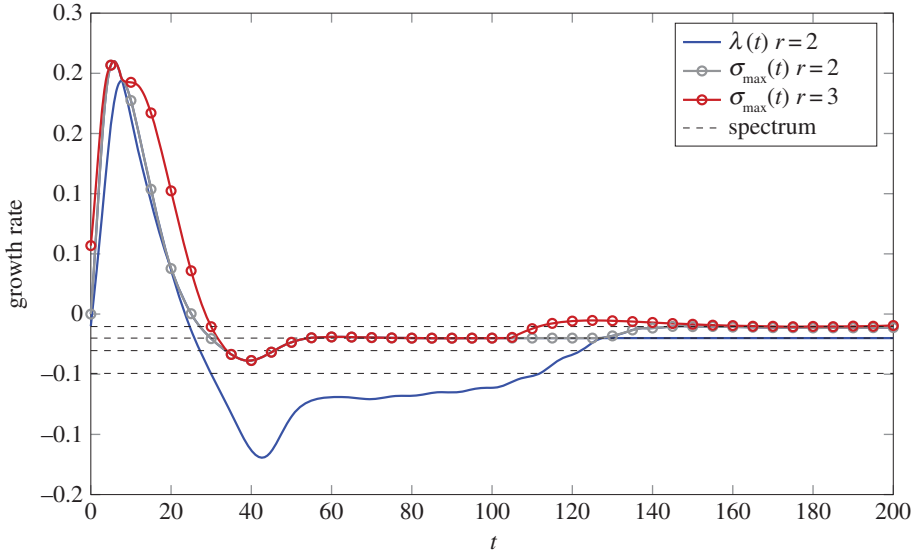

Figure 5. Plane Poiseuille flow at $Re = 5000$, $\alpha = 1$ and $\beta = 1$: instantaneous real eigenvalues with $r = 2$ (blue lines); numerical abscissa with $r = 2$ (grey lines); numerical abscissa with $r = 3$ (red); the real part of the first four least stable eigenvalues of the OS/SQ operator (dashed lines). (Online version in colour.)

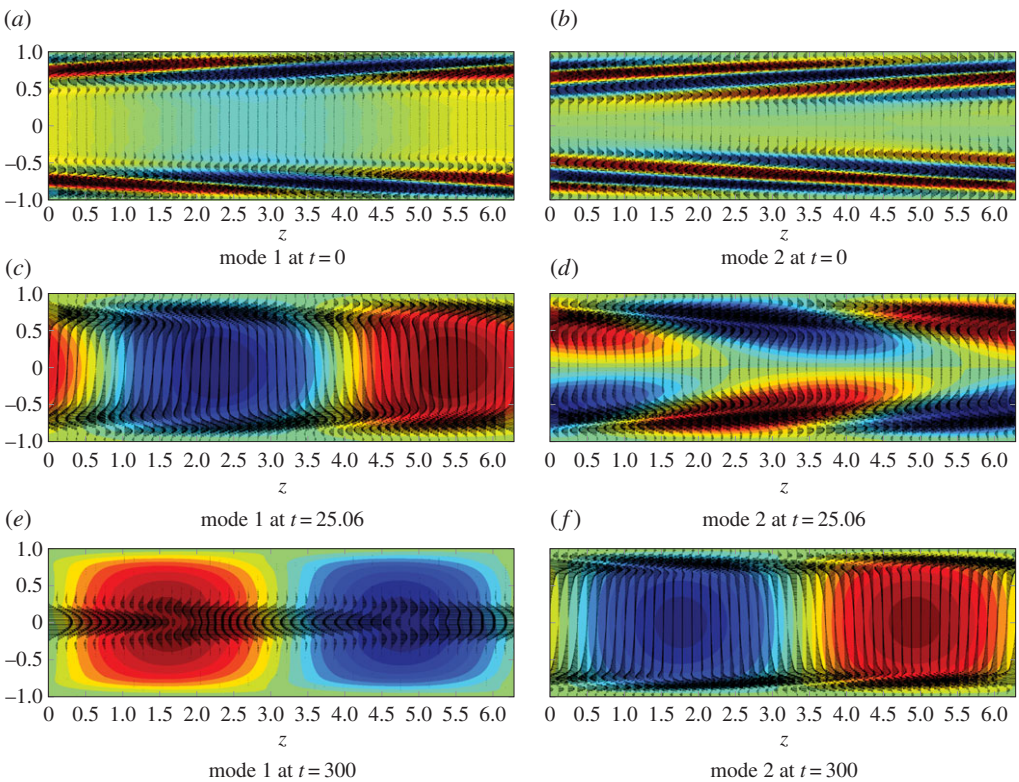

Figure 6. (*a*–*f*) Snapshots of the OTD modes with $r = 2$ at $Re = 5000$ and $\alpha = 1$ and $\beta = 1$ in the streamwise plane $x = \pi$. The contour shows the vertical velocity. (Online version in colour.)

large time $t = 300$. The initial state is marked by flow patterns that oppose the base shear. As time evolves from $t = 0$ to $t < t_{\max}$, the OTD modes tilt into the mean shear flow, resulting in significant growth rates for the subspace. At $t = 300$, the modes eventually approach the two most unstable eigenmodes of the OS/SQ operator. This demonstrates that the time-dependent modes capture characteristically different regimes in the evolution of the subspace.

4. Nonlinear dynamics

Here, we consider two nonlinear systems for which we compute the OTD modes. The first system is a low-dimensional dynamical system, while the second one is a more complex application involving an unstable flow with strongly transient characteristics.

(a) Low-dimensional dynamical system

We design a low-dimensional dynamical system in order to demonstrate transient growth over different directions and how these can be captured by the developed approach. In particular, we consider the following system:

$$\frac{\mathrm{d}z_1}{\mathrm{d}t} = -a_1 z_1 + \epsilon z_2 + b z_3, \tag{4.1}$$

$$\frac{\mathrm{d}z_2}{\mathrm{d}t} = \epsilon^{-1} z_1 - a_2 z_2 \tag{4.2}$$

and

$$\frac{\mathrm{d}z_3}{\mathrm{d}t} = b z_3 \left(\frac{1}{\sqrt{z_1^2 + z_2^2}} - 1 \right), \tag{4.3}$$

where we take $a_1 = a_2 = 2$, $\epsilon = 0.05$ and $b = 20$. For these parameters, the dynamical system has an almost periodic behaviour, where each cycle exhibits four distinct regimes: (1) a non-normal growth in the $z_1 - z_2$ plane, (2) exponential decay in the $z_1 - z_2$ plane to the origin, (3) an exponential growth in the z_3 direction, and (4) an exponential decay in the z_3 direction. In figure 7*a*, we present the trajectory of the dynamical system coloured according to the variable z_3 in the three-dimensional phase space. The four regimes as described above can be observed. We also present the projection of the vector field in the $z_3 = 0$ plane, where the non-normal structure can be seen as well. On the other hand, the singularity at $z_1^2 + z_2^2 = 0$ induces a severe exponential growth when the state approaches this region. This configuration allows for the repeated occurrence of non-normal and exponential instabilities.

We note that, due to the exponential instability close to the origin, the system undergoes chaotic transitions between positive and negative values of z_3. In figure 7*b*, we present a single cycle together with a single OTD mode (orange vector) shown for different time instants, while the time series for the state variables for one cycle is shown in figure 7*c*. The instantaneous growth rate σ corresponding to the computed OTD mode is shown in figure 7*d*. We can clearly observe that the OTD mode initially captures the severe exponential growth and subsequently captures the non-normal growth. On the other hand, the eigenvalues of the full linearized operator can only capture the exponential growth, even in regimes where it is not relevant, while they completely miss the non-normal growth.

(b) Vertical jet in cross-flow

The *jet in cross-flow* is an important problem in fluid mechanics with a wide range of applications from film cooling of gas turbines to pollutant dispersal from chimneys. The interplay of the jet and cross-flow creates coupled vortical structures whose interactions are highly unsteady and three dimensional, often leading to turbulence and resulting in a high-dimensional dynamical system [61]. The stability of the jet in cross-flow has been recently studied in [62], where an unstable base flow is computed by forcing the Navier–Stokes equation to an unstable steady

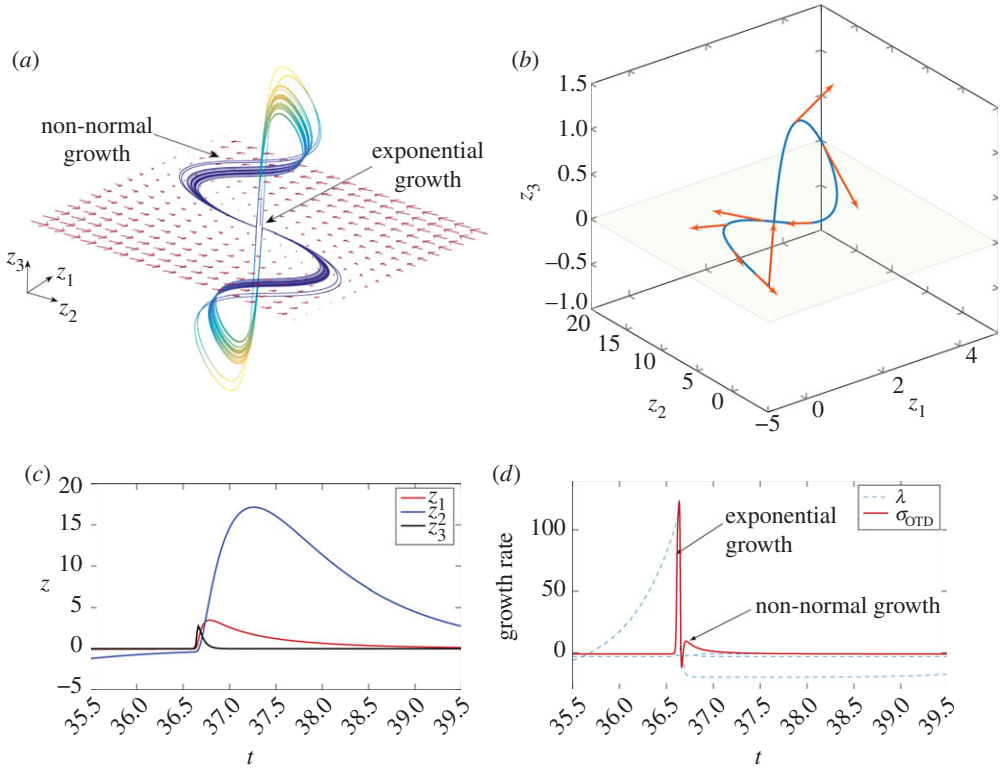

Figure 7. (*a*) A trajectory of the considered dynamical system coloured according to the state variable z_3. The non-normal vector field for $z_3 = 0$ is also shown. (*b*) A single cycle of the trajectory is shown together with a single OTD mode. (*c*) The time series for $z_i(t)$, $i = 1, 2, 3$. (*d*) The three eigenvalues of the linearized operator are plotted with blue dashed curves, while the growth rate of the single OTD mode is shown with orange colour. (Online version in colour.)

solution using the selective frequency damping method [63]. The Navier–Stokes equation is then linearized around the base flow, and the global eigenmodes of the linearized Navier–Stokes equation are then computed.

In this section, we compute the OTD modes for the vertical jet in cross-flow in a weakly turbulent regime. In particular, we follow the short- and long-time evolution of the OTD subspace with the *time-dependent base flow*, which is obtained by performing Direct Numerical Simulation (DNS) of the incompressible Navier–Stokes equation.

(i) Problem specification

The problem set-up is analogous to several recent studies in the literature [62,64]. A two-dimensional schematic of a vertical jet in cross-flow is shown in figure 8, where a vertical jet is issued into the cross-flow. The characteristic length is the displacement thickness of the cross-flow boundary layer. The origin of the coordinate system is placed at the centre of the jet exit with the jet diameter $D = 3\delta^*$. The computational domain spans from $x = -9.375\delta^*$ to $x = 55\delta^*$ in the streamwise direction, from $y = 0$ to $y = 50\delta^*$ in the wall-normal direction and from $z = -15\delta^*$ to $z = 15\delta^*$ in the spanwise direction.

At the cross-flow inlet, the Blasius boundary layer profile with the displacement thickness of δ^* and free-stream velocity of U_∞ is specified. The jet velocity profile is given by

$$v_{\mathrm{jet}}(r) = R(1 - r^2)\exp\left(-\left(\frac{r}{0.7}\right)^4\right), \tag{4.4}$$

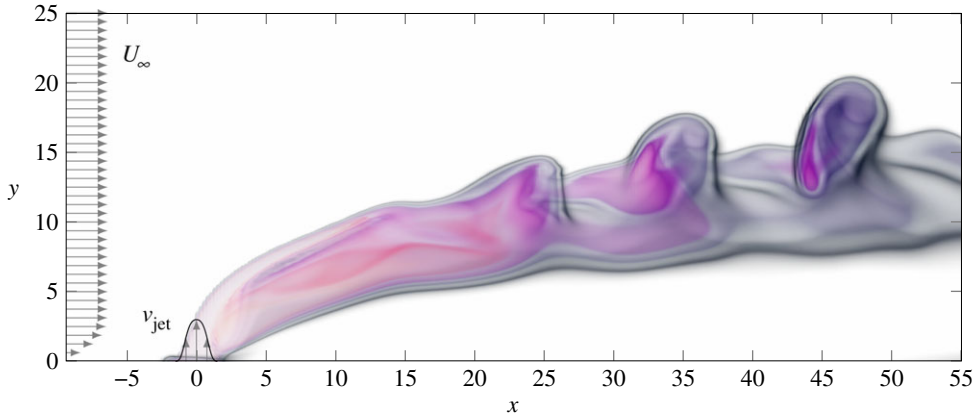

Figure 8. Schematic of the vertical jet in cross-flow in the x–y plane. A snapshot of the base flow is visualized by the volume rendering of the scalar field. (Online version in colour.)

where r is the normalized distance from the centre of the jet,

$$r = 2\sqrt{x^2 + z^2}/D,$$

and $R = V_j/U_\infty$ is the ratio of the *peak* jet velocity to the cross-flow velocity. The Reynolds number, based on the cross-flow velocity U_∞ and the displacement thickness, is given by $Re_\infty = U_\infty \delta^*/\nu$, while the jet Reynolds number is given by $Re_j = V_j D/\nu$. We use a velocity ratio $R = 3$, and a Reynolds number $Re_\infty = 100$ or equivalently $Re_j = 900$. At the top boundary, the free-stream velocity $\mathbf{U}_b = \{U_\infty, 0, 0\}$ is imposed. In the spanwise direction, periodic boundary conditions are used. At the outflow boundary, a zero-normal gradient is enforced for velocity components.

(ii) Optimally time-dependent equations for Navier–Stokes

To compute the time-dependent base flow, denoted by $\mathbf{U}_b := \mathbf{U}_b(\mathbf{x}, t)$, we solve the incompressible Navier–Stokes equation given by

$$\frac{\partial \mathbf{U}_b}{\partial t} + (\mathbf{U}_b \cdot \nabla)\mathbf{U}_b = -\nabla p_b + \frac{1}{Re}\nabla^2 \mathbf{U}_b \tag{4.5}$$

and

$$\nabla \cdot \mathbf{U}_b = 0, \tag{4.6}$$

along with the boundary conditions described in this section. The evolution equation for the modes is given by

$$\left.\begin{aligned} \frac{\partial \mathbf{u}_i}{\partial t} &= \mathcal{L}_{NS}(\mathbf{u}_i) - \langle \mathbf{u}_j, \mathcal{L}_{NS}(\mathbf{u}_i)\rangle \mathbf{u}_j \\ \text{and} \qquad \nabla \cdot \mathbf{u}_i &= 0, \end{aligned}\right\} \tag{4.7}$$

where $\mathcal{L}_{NS}$ is the linearized Navier–Stokes operator, given by

$$\mathcal{L}_{NS}(\mathbf{u}_i) = -(\mathbf{U}_b \cdot \nabla)\mathbf{u}_i - (\mathbf{u}_i \cdot \nabla)\mathbf{U}_b + \frac{1}{Re}\nabla^2 \mathbf{u}_i - \nabla p_i.$$

A zero boundary condition for $\mathbf{u}_i$, $i = 1, \ldots, r$ is enforced at the inflow, wall, jet exit and the top boundaries. Periodic boundary conditions are used in the spanwise direction and at the outflow, while zero-normal gradient is imposed on velocity components. In the above evolution equation,

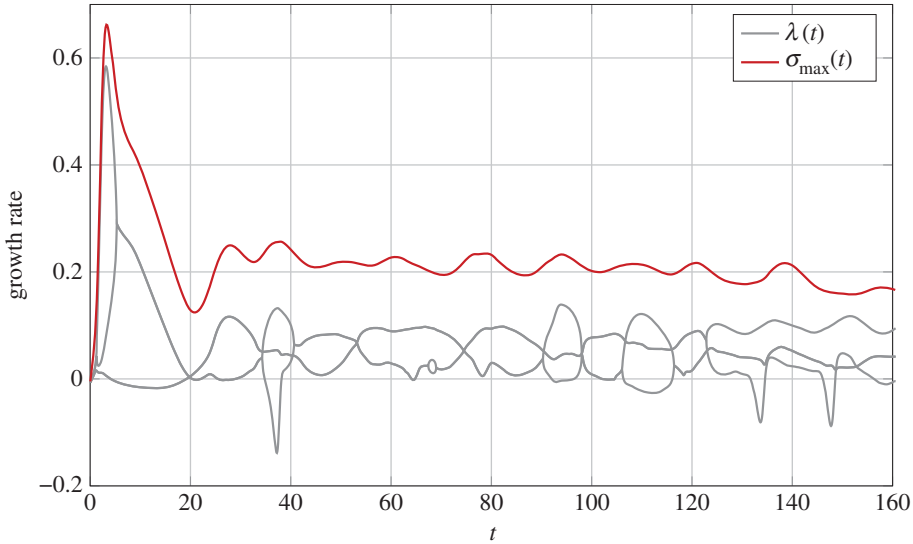

Figure 9. Instantaneous real eigenvalues and the numerical abscissa of the reduced operator (using the OTD modes), for the jet in cross-flow at $Re_j = 900$. (Online version in colour.)

the choice of the inner product is the second L_2 norm in the complex space

$$\langle \mathbf{u}, \mathbf{v} \rangle = \int_{\Omega} u_x v_x + u_y v_y + u_z v_z, \tag{4.8}$$

where $\mathbf{u} = (u_x, u_y, u_z)$ and $\mathbf{v} = (v_x, v_y, v_z)$ are the velocity vector fields. The reduced linear operator is therefore obtained from

$$L_{r_{ij}}(t) = \langle \mathbf{u}_i, \mathcal{L}_{NS}(\mathbf{u}_j) \rangle, \quad i, j = 1, \ldots, r. \tag{4.9}$$

(iii) Initial conditions

The initial condition for the modes is obtained by an orthonormalized space spanned by $\{\mathbf{u}_i(\mathbf{x})\}_{i=1}^{r}$ with $\mathbf{u}_i(\mathbf{x}) = (\partial\psi_i/\partial y, -\partial\psi_i/\partial x, 0)$, where the two-dimensional streamfunctions ψ_i are chosen as

$$\psi_i(x, y) = \sin(2\pi f_{x_i} x) \sin(2\pi f_{y_i} y) I(y), \tag{4.10}$$

where f_{x_i} and f_{y_i} are the wavenumbers and $\mathcal{I}(y)$ is a smooth indicator function, localizing the modes in the main body of the jet, i.e. between $y_s = 1.0$ and $y_e = 6.0$. More specifically, the indicator function is given by

$$I(y) = \tanh\left(\frac{(y - y_s)}{\delta}\right) - \tanh\left(\frac{(y - y_e)}{\delta}\right), \tag{4.11}$$

with $\delta = 0.5$. For the calculations that follow, we choose a four-dimensional OTD basis, i.e. $r = 4$.

(iv) Visualization

For the visualization of the base flow, we solve a passive scalar field θ that is governed by the advection–diffusion equation given by

$$\frac{\partial \theta}{\partial t} + (\mathbf{U}_b \cdot \nabla)\theta = \frac{1}{ReSc} \nabla^2 \theta,$$

where Sc is the Schmidt number and is chosen to be $Sc = 1$. The passive scalar is set to be $\theta = 1$ at the cross-flow inlet, $\theta = 0$ at the jet inlet, periodic condition at spanwise boundaries and zero

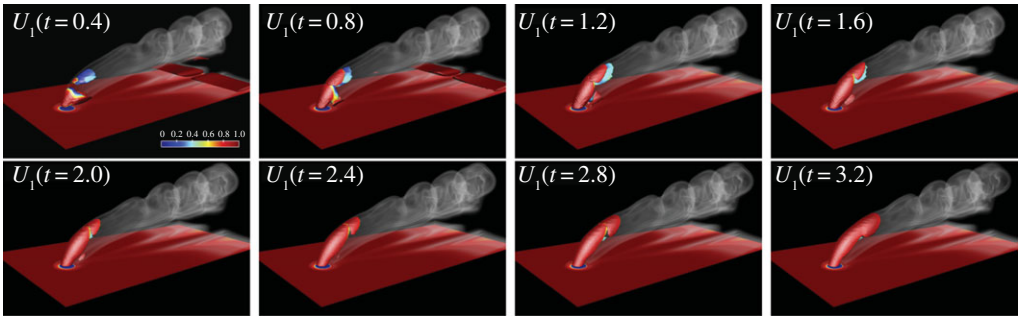

Figure 10. Initial evolution of the first mode and the trajectory of the Navier–Stokes equations, starting from $t = 0.4$ with the time advancement of $\Delta t = 0.4$ time units. The mode is visualized by the iso-surface of the velocity magnitude equal to 0.03. The time-dependent base flow (DNS) is visualized by smoke volume rendering of a scalar field. (Online version in colour.)

Neumann condition on all other boundaries. As such the jet body region is roughly determined by

$$\text{jet body} = \{\mathbf{x}, \text{such that } 0 \leq \theta(\mathbf{x}, t) < 1\}.$$

Moreover, by volume rendering only selected levels of θ, the shear layer and vortical structures can be revealed. In figure 8, the volume rendering of θ exposes the upper and lower shear layers above the jet exit, and also vortical structures further downstream. For visualizing the OTD modes, the iso-surface of the magnitude of velocity of the ranked OTD modes $\mathbf{U}_i$, coloured by the scalar field, is shown.

(v) Numerical algorithm

We use a spectral/hp element method to perform DNS of the full Navier–Stokes equation and the evolution equation for the OTD basis. The details of the spectral/hp element solver (NEKTAR) can be found in [65]. We use an unstructured hexahedral mesh with 99 792 elements with a spectral polynomial of order 4. For time integration, we use the splitting scheme with the first-order explicit Euler method with time increments of $\Delta t = 4 \times 10^{-3}$. The Navier–Stokes equations are first advanced for 200 time units, by which time the nonlinear dynamical system has reached a statistical steady state. Due to the inherent similarities of the evolution equations of the OTD basis to the nonlinear Navier–Stokes equation, the computational cost of solving a system of r OTD modes is roughly equal to r times of a single DNS run. Since the base flow is also solved along with the OTD modes, the total computational cost is $(r + 1)$ times of a single DNS run.

(vi) Non-normality and transient growth

In figure 9, the instantaneous real eigenvalues and the numerical abscissa of the reduced operator are shown. The large disparity between the numerical abscissa and the largest real eigenvalue of the reduced operator exposes a large degree of non-normality in the reduced operator L_r. The subspace experiences significant non-normal growth initially for $0 < t < 20$. This observation is qualitatively in accordance with the linear stability analysis of the jet in cross-flow in [62]. We refer the reader to fig. 3*c* in that article, in which the initial growth rate of the perturbation is much larger than its asymptotic behaviour.

The snapshots of the initial evolution of the first mode, i.e. the most unstable mode, are shown in figure 10. The mode is visualized by the iso-surface of the velocity magnitude equal to 0.03. At $t = 0.4$, the mode clearly captures both the lower and upper shear layers. As time advances, the presence of the upper shear layer becomes more pronounced. This is evident in the snapshots in the second row in figure 10. It should be remembered that the norm of each mode remains 1 for all times and, as a result, the mode quickly vanishes outside the jet body, where the magnitude of $\mathbf{U}_1(\mathbf{x}, t)$ is significantly smaller than the values in the shear layer regions.

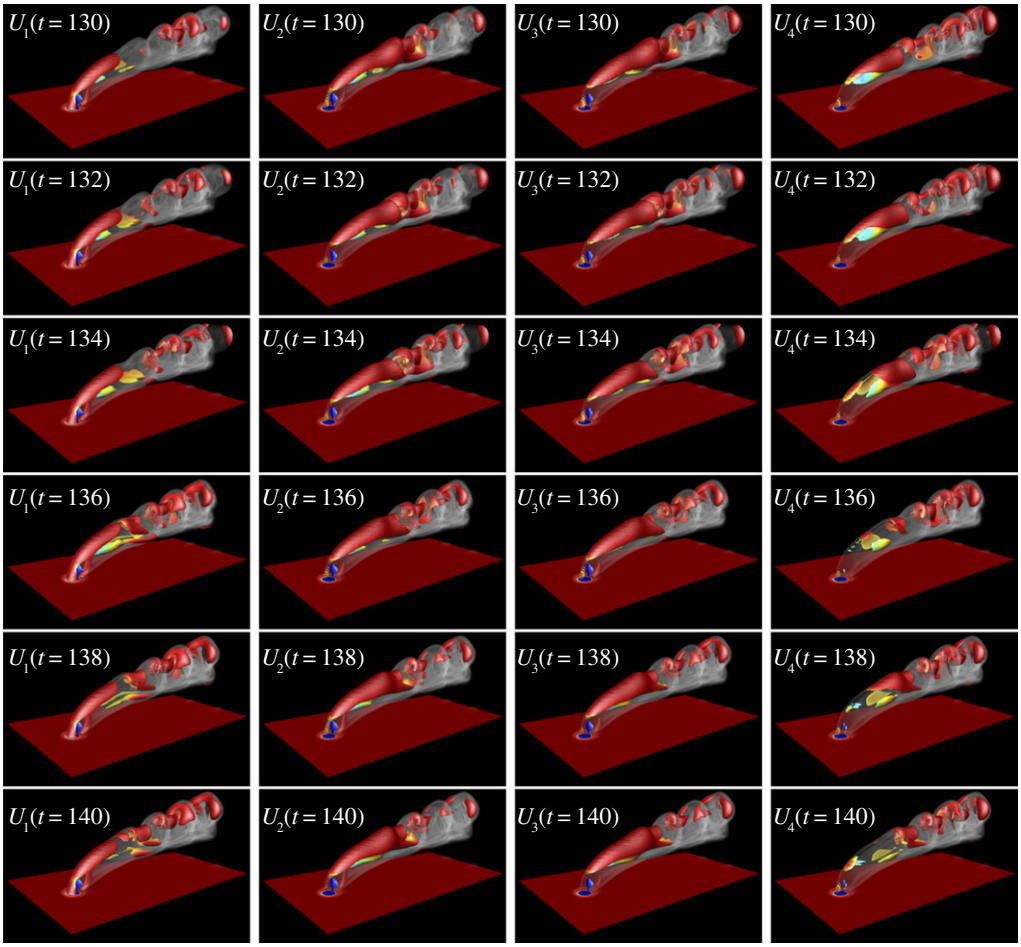

Figure 11. Snapshots of the OTD modes $\mathbf{U}_i(\mathbf{x}, t)$ and the trajectory of the Navier–Stokes equations. Each row shows all four modes at a given time, with the first row taken at $t = 130$. Time advancement from one row to the next is $\Delta t = 2$ time units. The modes are visualized by the iso-surface of the velocity magnitude equal to 0.02. The time-dependent base flow (DNS) is visualized by smoke volume rendering of a scalar field. (Online version in colour.)

(vii) Long-time behaviour

As time progresses, the subspace exhibits *bursts* of growth and sudden excursions into stable directions, as can be seen in figure 9. At each time instant at least one or more unstable directions can be observed. These unstable directions appear either singly (real eigenvalues) or in pairs (complex conjugate eigenvalues). The unstable directions represent *persistent instabilities* that are the hallmark of shear flows.

In figure 11, the snapshots of all four modes along with the smoke volume rendering of the Navier–Stokes equation are shown. The modes are visualized by iso-surfaces of the velocity magnitude (equal to 0.02) and coloured by the scalar field θ. Each column tracks one mode at different time instants, starting from the top row at $t = 120$, with the time advancement of $\Delta t = 2$ to the next row. The modes are sorted from the most unstable directions (mode 1) to the most stable directions (mode 4). The first mode captures the *vortex sheet* in the upper shear layer of the jet. This reaffirms the strong evidence that the jet upper shear layer is unstable, leading to the vortex roll-up further downstream [62]. The second and the third modes show strong presence in both the upper and lower shear layers, while the fourth mode captures the dominant vortical structures downstream.

The shear layer, spanned by the OTD subspace, is a critical dynamical feature since it is associated with the 'birth place' of the instability. The strong presence of the upper and lower shear layers in the large times exposes the important role of non-normality even in the asymptotic dynamics of this flow. Moreover, the upper shear layer remains almost steady and as such it has negligible turbulent kinetic energy. Therefore, in energy-based reduction techniques such as proper orthogonal decomposition, the shear layer appears strongly in the time-averaged fields, and only weakly with modes with which unstable directions are associated. A more comprehensive analysis of the origin of the modes and their connection with coherent structures is currently in progress.

5. Conclusion

We have introduced a minimization formulation for the extraction of a finite-dimensional, time-dependent, orthonormal basis, which captures directions of the phase space associated with transient instabilities. The central idea is to build a set of OTD modes with a rate of change that optimally spans the vector field of the full dynamical system, in the neighbourhood of its current state. We demonstrated how the formulated minimization principle can be used to produce evolution equations for these time-dependent modes. These equations require a trajectory of the system as well as the linearized operator and their solution gives a time-dependent orthonormal basis which spans the current directions (i.e. for the current state of the system) associated with maximum growth. For the special case of equilibrium states, we have shown that these modes rapidly converge to the most unstable directions of the system.

We have demonstrated the capability of the approach in capturing instabilities caused by linear dynamics such as non-normal effects as well as nonlinear exchanges of energy between modes. In particular, we have illustrated the computation of the OTD modes in order to capture energy growth/exchanges occurring in: (i) linear systems including the advection–diffusion operator in a strongly non-normal regime as well as the Orr–Sommerfeld/Squire operator and (ii) nonlinear systems including a low-dimensional system with both non-normal and exponential growth regimes, and the vertical jet in cross-flow in an unstable regime. For the linear systems, we demonstrated that the time-dependent subspace captures the strongly transient non-normal energy growth (in the short-time regime), while for longer times the modes capture the expected asymptotic behaviour of the dynamics. For the low-dimensional nonlinear system, we demonstrated how the subspace captures the most unstable directions of the dynamics, associated with exponential or non-normal growth, while for the fluid flow example we also explored the connection between the shear flow, non-normal growth and persistent instabilities.

The proposed approach paves the way for (i) the formulation of efficient, reduced-order filtering and prediction schemes for a variety of infinite dimensional problems involving strongly transient features, such as rare events, and (ii) the formulation of low-energy control algorithms that will be able to suppress the instability at a very early stage by applying reduced-order control methods the moment that the instability has begun to emerge. The proposed framework should also be important for the fundamental understanding of the dynamical processes behind transient features, through the computation of finite-time Lyapunov exponents (a task that is not feasible in an infinite dimensional setting) and the analysis of the associated energy transfers. Additional conditions or constraints on the definition of the OTD modes, such as minimal or low torsion of the modes, may be considered and this is part of future work.

Data accessibility. The paper contains no data other than that already present in the body of the paper.

Authors' contributions. H.B. and T.P.S. designed and performed the research and drafted the manuscript. All authors gave final approval for publication.

Competing interests. We declare we have no competing interests linked to this study.

Funding. T.P.S. has been supported through the Army Research Office Young Investigator Award 66710-EG-YIP, the Office of Naval Research grant no. ONR N00014-14-1-0520 and the DARPA grant no. HR0011-14-1-0060. H.B. has been partially supported as a post-doc by the first and third grants.

Acknowledgements. The authors thank Prof. Karniadakis, Dr Farazmand and Mr Mowlavi for useful comments that led to a number of improvements. T.P.S. thanks Prof. Majda and Prof. Kevrekidis for numerous stimulating discussions. The authors gratefully acknowledge the allocated computer time on the Stampede supercomputers, awarded by the XSEDE Program, allocation no. TG-ECS140006.

References

1. Chandler GJ, Kerswell RR. 2013 Invariant recurrent solutions embedded in a turbulent two-dimensional Kolmogorov flow. *J. Fluid Mech.* **722**, 554–595. (doi:10.1017/jfm.2013.122)
2. Hamilton JM, Kim J, Waleffe F. 1995 Regeneration mechanisms of near-wall turbulence structures. *J. Fluid Mech.* **287**, 243. (doi:10.1017/S0022112095000978)
3. Smooke MD, Mitchell RE, Keyes DE. 1986 Numerical solution of two-dimensional axisymmetric laminar diffusion flames. *Combust. Sci. Technol.* **67**, 85–122. (doi:10.1080/00102208908924063)
4. Pope SB. 1997 Computationally efficient implementation of combustion chemistry using 'in situ' adaptive tabulation. *Combust. Theory Modell.* **1**, 41–63. (doi:10.1080/713665229)
5. Majda AJ. 2012 Challenges in climate science and contemporary applied mathematics. *Commun. Pure Appl. Math.* **65**, 920. (doi:10.1002/cpa.21401)
6. Majda AJ. 2000 Real world turbulence and modern applied mathematics. In *Mathematics: frontiers and perspectives* (eds V Arnold, M Atiyah, P Lax, B Mazur), pp. 137–151. International Mathematical Union. Providence, RI: American Mathematical Society.
7. Grabowski WW, Smolarkiewicz PK. 1999 CRCP: a Cloud Resolving Convection Parameterization for modeling the tropical convecting atmosphere. *Phys. D Nonlinear Phenom.* **133**, 171–178. (doi:10.1016/S0167-2789(99)00104-9)
8. Grabowski WW. 2001 Coupling cloud processes with the large-scale dynamics using the cloud-resolving convection parameterization (CRCP). *J. Atmos. Sci.* **58**, 978–997. (doi:10.1175/1520-0469(2001)058<0978:CCPWTL>2.0.CO;2)
9. Akhmediev N, Dudley JM, Solli DR, Turitsyn SK. 2013 Recent progress in investigating optical rogue waves. *J. Opt.* **15**, 60201. (doi:10.1088/2040-8978/15/6/060201)
10. Arecchi FT, Bortolozzo U, Montina A, Residori S. 2011 Granularity and inhomogeneity are the joint generators of optical rogue waves. *Phys. Rev. Lett.* **106**, 2–5. (doi:10.1103/PhysRevLett.106.153901)
11. Onorato M, Residori S, Bortolozzo U, Montina A, Arecchi FT. 2013 Rogue waves and their generating mechanisms in different physical contexts. *Phys. Rep.* **528**, 47–89. (doi:10.1016/j.physrep.2013.03.001)
12. Muller P, Garrett C, Osborne A. 2005 Rogue waves. *Oceanography* **18**, 66–75. (doi:10.5670/oceanog.2005.30)
13. Cousins W, Sapsis TP. 2015 The unsteady evolution of localized unidirectional deep water wave groups. *Phys. Rev. E* **91**, 063204. (doi:10.1103/PhysRevE.91.063204)
14. Cousins W, Sapsis TP. In press. Reduced order prediction of rare events in unidirectional nonlinear water waves. *J. Fluid Mech.*
15. Mohamad MA, Sapsis TP. 2015 Probabilistic description of extreme events in intermittently unstable systems excited by correlated stochastic processes. *SIAM ASA J. Uncertain. Quantification* **3**, 709–736. (doi:10.1137/140978235)
16. Arnold L, Chueshov I, Ochs G. 2004 Stability and capsizing of ships in random sea: a survey. *Nonlinear Dyn.* **36**, 135–179. (doi:10.1023/B:NODY.0000045506.30721.f2)
17. Kourdis PD, Vakakis AF. 2006 Some results on the dynamics of the linear parametric oscillator with general time-varying frequency. *Appl. Math. Comput.* **183**, 1235–1248. (doi:10.1016/j.amc.2006.06.049)
18. Mohamad MA, Sapsis TP. In press. Probabilistic response and rare events in Mathieu's equation under correlated parametric excitation. *Ocean Eng. J.*
19. Haller G, Sapsis T. 2010 Localized instability and attraction along invariant manifolds. *SIAM J. Appl. Dyn. Syst.* **9**, 611–633. (doi:10.1137/08074324X)
20. Schmid PJ. 2007 Nonmodal stability theory. *Annu. Rev. Fluid Mech.* **39**, 129–162. (doi:10.1146/annurev.fluid.38.050304.092139)
21. Tantet A, van der Burgt FR, Dijkstra HA. 2015 An early warning indicator for atmospheric blocking events using transfer operators. *Chaos* **25**, 036406. (doi:10.1063/1.4908174)
22. Susuki Y, Mezic I. 2014 Nonlinear Koopman modes and power system stability assessment without models. *IEEE Trans. Power Syst.* **29**, 899–907. (doi:10.1109/TPWRS.2013.2287235)

23. Susuki Y, Mezić I. 2012 Nonlinear Koopman modes and a precursor to power system swing instabilities. *IEEE Trans. Power Syst.* **27**, 1182–1191. (doi:10.1109/TPWRS.2012.2183625)
24. Cousins W, Sapsis TP. 2014 Quantification and prediction of extreme events in a one-dimensional nonlinear dispersive wave model. *Physica D* **280**, 48–58. (doi:10.1016/j.physd.2014.04.012)
25. Pastoor M, Henning L, Noack BR, King R, Tadmor G. 2008 Feedback shear layer control for bluff body drag reduction. *J. Fluid Mech.* **608**, 161–196.
26. Tadmor G, Lehmann O, Noack BR, Cordier L, Delville J, Bonnet JP, Morzynski M. 2011 Reduced order models for closed-loop wake control. *Phil. Trans. R. Soc. A* **369**, 1513–1524. (doi:10.1098/rsta.2010.0367)
27. Cornelius SP, Kath WL, Motter AE. 2013 Realistic control of network dynamics. *Nat. Commun.* **4**, 1942. (doi:10.1038/ncomms2939)
28. Böberg L, Brösa U. 1988 Onset of turbulence in a pipe. *Z. Nat. A.* **43a**, 697–726. (doi:10.1515/zna-1988-8-901)
29. Butler KM, Farrell BF. 1992 Three dimensional optimal perturbations in viscous shear flow. *Phys. Fluids A* **4**, 1637–1650. (doi:10.1063/1.858386)
30. Trefethen LN, Trefethen AE, Reddy SC, Driscoll TA. 1993 Hydrodynamic stability without eigenvalues. *Science* **261**, 578–584. (doi:10.1126/science.261.5121.578)
31. Trefethen LN. 1997 Pseudospectra of linear operators. *SIAM Rev.* **39**, 383–406. (doi:10.1137/S0036144595295284)
32. Reddy SC, Schmid PJ, Henningson DS. 1993 Pseudospectra of the Orr-Sommerfeld operator. *SIAM J. Appl. Math.* **53**, 15–47. (doi:10.1137/0153002)
33. Schmid PJ. 2000 Linear stability theory and bypass transition in shear flows. *Phys. Fluids* **7**, 1788–1794. (doi:10.1063/1.874049)
34. Grossmann S. 2000 The onset of shear flow turbulence. *Rev. Mod. Phys.* **72**, 603–618. (doi:10.1103/RevModPhys.72.603)
35. Henningson DS, Lundbladh A, Johansson AV. 1993 A mechanism for bypass transition from localized disturbances in wall-bounded shear flows. *J. Fluid Mech.* **250**, 169–207. (doi:10.1017/S0022112093001429)
36. Moxey D, Barkley D. 2010 Distinct large-scale turbulent-laminar states in transitional pipe flow. *Proc. Natl Acad. Sci. USA* **107**, 8091–8096. (doi:10.1073/pnas.0909560107)
37. Avila K, Moxey D, Alberto LD, Avila M, Barkley D, Hof B. 2011 The onset of turbulence in pipe flow. *Science* **333**, 192–196. (doi:10.1126/science.1203223)
38. Egolf DA, Melnikov IV, Pesch W, Ecke RE. 2000 Mechanisms of extensive spatiotemporal chaos in Rayleigh–Bénard convection. *Nature* **404**, 733–736. (doi:10.1038/35008013)
39. Majda AJ, Branicki M. 2012 Lessons in uncertainty quantification for turbulent dynamical systems. *Discret. Contin. Dyn. Syst.* **32**, 3133–3221. (doi:10.3934/dcds.2012.32.3133)
40. Branicki M, Majda AJ. 2012 Quantifying uncertainty for predictions with model error in non-Gaussian systems with intermittency. *Nonlinearity* **25**, 2543. (doi:10.1088/0951-7715/25/9/2543)
41. Majda AJ, Harlim J. 2012 *Filtering complex turbulent systems*. Cambridge, UK: Cambridge University Press.
42. Bourlioux A, Majda AJ. 2002 Elementary models with probability distribution function intermittency for passive scalars with a mean gradient. *Phys. Fluids* **14**, 881–897. (doi:10.1063/1.1430736)
43. Bourlioux A, Majda AJ, Volkov O. 2006 Conditional statistics for a passive scalar with a mean gradient and intermittency. *Phys. Fluids* **18**, 1–10. (doi:10.1063/1.2353880)
44. Tong X, Majda AJ. 2015 Intermittency in turbulent diffusion models with a mean gradient. *Nonlinearity* **28**, 4171–4208. (doi:10.1088/0951-7715/28/11/4171)
45. Sapsis TP, Lermusiaux PFJ. 2009 Dynamically orthogonal field equations for continuous stochastic dynamical systems. *Physica D* **238**, 2347–2360. (doi:10.1016/j.physd.2009.09.017)
46. Sapsis TP, Lermusiaux PFJ. 2012 Dynamical criteria for the evolution of the stochastic dimensionality in flows with uncertainty. *Physica D* **241**, 60. (doi:10.1016/j.physd.2011.10.001)
47. Cheng M, Hou T, Zhang Z. 2013 A dynamically bi-orthogonal method for time-dependent stochastic PDEs I: derivation and algortihms. *J. Comput. Phys.* **242**, 843–868. (doi:10.1016/j.jcp.2013.02.033)
48. Sapsis TP. 2013 Attractor local dimensionality, nonlinear energy transfers, and finite-time instabilities in unstable dynamical systems with applications to 2D fluid flows. *Proc. R. Soc. A* **469**, 20120550. (doi:10.1098/rspa.2012.0550)

49. Sapsis TP, Dijkstra HA. 2013 Interaction of noise and nonlinear dynamics in the double-gyre wind-driven ocean circulation. *J. Phys. Oceanogr.* **43**, 366–381. (doi:10.1175/JPO-D-12-047.1)
50. Sapsis TP, Ueckermann MP, Lermusiaux PFJ. 2013 Global analysis of Navier–Stokes and Boussinesq stochastic flows using dynamical orthogonality. *J. Fluid Mech.* **734**, 83–113. (doi:10.1017/jfm.2013.458)
51. Sapsis TP, Majda AJ. 2013 A statistically accurate modified quasilinear Gaussian closure for uncertainty quantification in turbulent dynamical systems. *Physica D* **252**, 34–45. (doi:10.1016/j.physd.2013.02.009)
52. Sapsis TP, Majda AJ. 2013 Blended reduced subspace algorithms for uncertainty quantification of quadratic systems with a stable mean state. *Physica D* **258**, 61. (doi:10.1016/j.physd.2013.05.004)
53. Majda AJ, Qi D, Sapsis TP. 2014 Blended particle filters for large-dimensional chaotic dynamical systems. *Proc. Natl Acad. Sci. USA* **111**, 7511–7516. (doi:10.1073/pnas.1405675111)
54. Sapsis TP, Majda AJ. 2013 Statistically accurate low-order models for uncertainty quantification in turbulent dynamical systems. *Proc. Natl Acad. Sci. USA* **110**, 13 705–13 710. (doi:10.1073/pnas.1313065110)
55. Sapsis TP, Majda AJ. 2013 Blending modified Gaussian closure and non-Gaussian reduced subspace methods for turbulent dynamical systems. *J. Nonlinear Sci.* **23**, 1039–1071. (doi:10.1007/s00332-013-9178-1)
56. Qi D, Majda AJ. 2015 Blended particle methods with adaptive subspaces for filtering turbulent dynamical systems. *Physica D* **299**, 21–41. (doi:10.1016/j.physd.2015.02.002)
57. Farrell BF, Ioannou PJ. 1996 Generalized stability theory. Part II: non-autonomous operators. *J. Atmos. Sci.* **53**, 2041–2053. (doi:10.1175/1520-0469(1996)053<2041:GSTPIN>2.0.CO;2)
58. Driscoll TA, Hale N, Trefethen LN 2014 *Chebfun guide: technical report*. Oxford, UK: Pafnuty Publications.
59. Schmid PJ, Henningson DS. 2001 *Stability and transition stability in shear flows*. New York, NY: Springer.
60. Orszag SA. 1971 Accurate solution of the Orr-Sommerfeld stability equation. *J. Fluid Mech.* **50**, 689–703. (doi:10.1017/S0022112071002842)
61. Babaee H. 2013 Analysis and optimization of film cooling effectiveness. PhD thesis, Louisiana State University, Baton Rouge, LA, USA.
62. Bagheri S, Schlatter P, Schmid PJ, Henningson DS. 2009 Global stability of a jet in crossflow. *J. Fluid Mech.* **624**, 33–44. (doi:10.1017/S0022112009006053)
63. Åkervik E, Brandt L, Henningson DS, Hœpffner J, Marxen O, Schlatter P. 2006 Steady solutions of the Navier–Stokes equations by selective frequency damping. *Phys. Fluids* **18**, 068102. (doi:10.1063/1.2211705)
64. Babaee H. 2013 Uncertainty quantification of film cooling effectiveness in gas turbines. Master's thesis, Louisiana State University, Baton Rouge, LA, USA.
65. Karniadakis GE, Sherwin SJ. 2005 *Spectral/hp element methods for computational fluid dynamics*. New York, NY: Oxford University Press.